Monthly Notices of the ROYAL ASTRONOMICAL SOCIETY

MNRAS **533,** 2454–2472 (2024) https://doi.org/10.1093/mnras/stae1912
Advance Access publication 2024 August 7

An attractive model: simulating fuzzy dark matter with attractive self-interactions

Connor A. Painter [1]★ Michael Boylan-Kolchin [1] Philip Mocz [2,3] and Mark Vogelsberger [4]

[1]*Department of Astronomy, The University of Texas at Austin, 2515 Speedway, Stop C1400, Austin, TX 78712-1205, USA*
[2]*Lawrence Livermore National Laboratory, 7000 East Ave, Livermore CA 94550, USA*
[3]*Department of Astrophysical Sciences, Princeton University, 4 Ivy Lane, Princeton, NJ 08544, USA*
[4]*Department of Physics, Kavli Institute for Astrophysics and Space Research, M.I.T., Cambridge, MA 02139, USA*

Accepted 2024 July 31. Received 2024 June 28; in original form 2024 February 26

ABSTRACT

Fuzzy dark matter (FDM), comprised of ultralight ($m \sim 10^{-22}$ eV) boson particles, has received significant attention as a viable alternative to cold dark matter (CDM), as it approximates CDM on large scales ($\gtrsim$1 Mpc) while potentially resolving some of its small-scale problems via kiloparsec-scale quantum interference. However, the most basic FDM model, with one free parameter (the boson mass), is subject to a tension: small boson masses yield the desired cores of dwarf galaxies but underpredict structure in the Lyman-α forest, while large boson masses render FDM effectively identical to CDM. This *Catch-22* problem may be alleviated by considering an axion-like particle with attractive particle self-interactions. We simulate an idealized FDM halo with self-interactions parametrized by an energy decay constant $f \sim 10^{15}$ GeV related to the axion symmetry-breaking conjectured to solve the strong-CP problem in particle physics. We observe solitons, a hallmark of FDM, condensing within a broader halo envelope, and find that the density profile and soliton mass depend on self-interaction strength. We propose generalized formulae to extend those from previous works to include self-interactions. We also investigate a critical mass threshold predicted for strong interactions at which the soliton collapses into a compact, unresolved state. We find that the collapse happens quickly, and its effects are initially contained to the central region of the halo.

Key words: galaxies: formation – galaxies: high-redshift – dark matter – cosmology: theory.

1 INTRODUCTION

The particle nature of cosmological dark matter is still one of the most pressing unknowns in modern astrophysics. For decades, cold dark matter (CDM) has prevailed as the leading theory, stating that dark matter particles are non-relativistic, collisionless, and dissipationless. CDM, as part of the ΛCDM paradigm, has reproduced observations of the cosmic microwave background (Aghanim et al. 2020; Alam et al. 2021) and large-scale structure remarkably well (Schaye et al. 2014; Vogelsberger et al. 2014a, b; Springel et al. 2017; Vogelsberger et al. 2020). However, the simplest CDM simulations admit puzzling discrepancies with observations on the scale of dwarf galaxies (Bullock & Boylan-Kolchin 2017; Del Popolo & Le Delliou 2017; Sales, Wetzel & Fattahi 2022). Problems actively debated in the literature include missing satellites (Klypin et al. 1999; Moore et al. 1999), density profile cores versus cusps (Flores & Primack 1994; Moore 1994; de Blok 2010), dark matter haloes 'too big to fail' to produce stars (Boylan-Kolchin, Bullock & Kaplinghat 2011; Garrison-Kimmel et al. 2014), and overly diverse galaxy rotation curves (Oman et al. 2015). Even though baryonic feedback has shown promise to remedy many of the inconsistencies when incorporated into ΛCDM simulations, the most commonly considered CDM particle candidates, weakly interacting massive particles (WIMPs) on the mass scale of GeV, have so far evaded discovery (Roszkowski, Sessolo & Trojanowski 2018). Small-scale inconsistencies, along with non-detections of plausible particle candidates, have fuelled a search for alternative models.

A popular alternative to CDM is dark matter in the form of ultra-light boson particles of mass $m \sim 10^{-22}$ eV (Hu, Barkana & Gruzinov 2000; Guzmán & Ureña-López 2003; Hui et al. 2017; Mocz et al. 2019; Burkert 2020; Niemeyer 2020; Hui 2021). This so-called fuzzy dark matter (FDM) model approximates CDM on large scales (Widrow & Kaiser 1993; Kopp, Vattis & Skordis 2017), but small-scale structure is altered by a 'quantum pressure' tensor in the momentum equation (Schive, Chiueh & Broadhurst 2014a). The dark matter clusters under self-gravity with fluid-like properties, and dark waves generated on the de Broglie scale $\lambda_{\rm dB} \equiv \frac{h}{mv} \sim$ kpc interfere to smooth over small-scale structure. This smoothing cuts off the dark matter power spectrum above a certain wavenumber (Hu et al. 2000), offering a natural explanation for the missing satellites predicted by CDM-only simulations. FDM also naturally addresses the cusp-core discrepancy: haloes are characterized by cored central structures called *solitons* (Schive et al. 2014a; Schive et al. 2014b) enveloped by a broader Navarro–Frenk–White (NFW)-like power law drop-off in density (Navarro, Frenk & White 1996; Marsh & Pop 2015; Mocz et al. 2017). Furthermore, ultra-light bosons are predicted to arise naturally in many string theory models (Svrcek &

★ E-mail: connor.painter@austin.utexas.edu

Witten 2006) and their present-day energy density in the Universe could be comparable to the measured dark matter density (Arvanitaki et al. 2010; Marsh 2016; Hui et al. 2017).

These convenient properties of the FDM model have generated excitement and substantial investigation in the literature. In recent years, for example, FDM has been simulated both in high resolution on cosmological scales to characterize structure formation (Woo & Chiueh 2009; Mocz et al. 2019, 2020; Laguë et al. 2021; May & Springel 2021; Nori & Baldi 2021; Schwabe & Niemeyer 2022; Dome et al. 2023; Huang, Schive & Chiueh 2023; Laguë et al. 2024; Shen et al. 2024) and on scales of individual haloes in idealized scenarios (Mocz et al. 2017; Du et al. 2018; Schwabe et al. 2020; Veltmaat, Schwabe & Niemeyer 2020; Li, Hui & Yavetz 2021). In the simplest FDM model, the shape of a cosmological soliton is related to its total mass and the boson mass (Schive et al. 2014a), and some regions of parameter space are capable of matching observations of dwarf galaxies (Marsh & Pop 2015; Luu, Tye & Broadhurst 2020; Safarzadeh & Spergel 2020). For a recent mini-review of the achievements of FDM, see Matos, Ureña-López & Lee (2024).

However, the simple FDM model struggles to simultaneously reproduce the power spectrum of the Lyman-α forest and the core sizes of dwarf galaxies (Iršič et al. 2017; Nori et al. 2019; Dome, Azhar & Fialkov 2024). Lower boson masses ($m < 1.1 \times 10^{-22}$ eV at 2σ C.L., Marsh & Pop 2015) are required to yield the desired cores of satellite galaxies, but higher masses ($m > 2.0 \times 10^{-21}$ eV at 2σ C.L., Iršič et al. 2017) are required to predict adequate small-scale structure in the Lyman-α forest. Constraints from the two observations leave little to no overlap. There is some discussion (e.g. Elgamal et al. 2024) suggesting that 'vanilla' FDM is still capable of fitting observations of both Lyman-α structure and dwarf galaxies, but this *Catch-22* (Davies & Mocz 2020) is widely regarded to be a serious challenge. Other constraints on FDM models come from strong lensing (Shevchuk, Kovetz & Zitrin 2023), ultrafaint dwarfs (Hayashi, Ferreira & Chan 2021; Dalal & Kravtsov 2022), dynamical friction (Foote et al. 2023), and cosmology (Li, Rindler-Daller & Shapiro 2014; Li, Shapiro & Rindler-Daller 2017).

The *Catch-22* may be alleviated by introducing a second degree of freedom through a scalar potential term that naturally arises if the FDM particle is an ultralight *axion-like particle* (Arvanitaki et al. 2020; Mocz et al. 2023). Ultralight axions are natural outcomes of particle physics models that solve the longstanding 'strong CP problem' in quantum chromodynamics (QCD) (Peccei & Quinn 1977; Weinberg 1978). In these models of FDM, the axion-like particle typically has a decay constant (or symmetry-breaking scale) $f \sim 10^{17}$ GeV present in an additional scalar potential term in its governing equations. This new potential term will instigate attractive interparticle self-interactions (SI). These interactions are extremely weak, with quartic coupling $m^2/f^2 \sim 10^{-96}$, but theoretical and numerical work suggest that they may have non-negligible impacts on cosmic structure at low redshift (Desjacques, Kehagias & Riotto 2018; Mocz et al. 2023). In particular, attractive self-interactions introduce a critical mass scale for FDM haloes above which the soliton collapses into an extremely compact state (Chavanis 2011; Chavanis & Delfini 2011), a process that may bolster small-scale structure enough to match observations of the Lyman-α forest (Mocz et al. 2023).

Recent simulations have begun to characterize the extent to which axion-like self-interactions change FDM predictions. Amin & Mocz (2019) carried out cosmological simulations of FDM with attractive SI to examine soliton formation and gravitational clustering. Chen et al. (2021) simulated isolated clusters of FDM haloes with both attractive and repulsive self-interactions. Glennon & Prescod-Weinstein (2021) simulated idealized solitons with attractive SI, verifying criteria for soliton collapse and quantifying changes in tidal stripping time-scales. Mocz et al. (2023) used cosmological simulations to gauge the extent to which weak attractive self-interactions enhance small-scale structure in the cosmic web. Jain & Amin (2023) published an integrator for FDM systems with general self-interactions. Besides attractive self-interactions, other extensions of FDM explored in the literature include repulsive self-interactions (Dawoodbhoy, Shapiro & Rindler-Daller 2021; Shapiro, Dawoodbhoy & Rindler-Daller 2022), multifield FDM (Eby et al. 2020; Luu et al. 2020; Guo et al. 2021; Huang et al. 2023; Luu et al. 2024), mixed CDM and FDM (Schwabe et al. 2020; Laguë et al. 2024), FDM with a large initial misalignment angle (Zhang & Chiueh 2017; Schive & Chiueh 2018), and vector dark matter, where FDM is a higher-spin field (Amin et al. 2022).

The purpose of this work is to provide a careful analysis of the interior structure of FDM haloes under attractive self-interactions in idealized simulations. We pay particular attention to the regime of weak SI, in which the soliton is noticeably influenced, but not so much that it exceeds the critical mass and collapses. This work informs the analysis of future cosmological simulations of FDM with attractive self-interactions that seek to break the *Catch-22*.

The rest of this paper is organized as follows: In Section 2, we review the governing equations of FDM, modify them to include self-interactions, and solve them under spherical symmetry to formulate predictions for halo density profiles. In Section 3, we describe the idealized halo simulations we perform to study the effects of including self-interactions. In Section 4, we present analysis and trends between simulations with varying SI strengths. We contextualize and conclude the work in Sections 5 and 6.

2 PHYSICAL EQUATIONS

In the non-relativistic limit, self-interacting FDM is governed by the Gross–Pitaevskii–Poisson (GPP) equations,

$$i\hbar\left(\frac{\partial}{\partial t}\right)\psi = \left(-\frac{\hbar^2}{2m}\nabla^2 + mV - \frac{4\pi\hbar^2 a_s}{m^2}\rho\right)\psi \tag{1}$$

$$\nabla^2 V = 4\pi G(\rho - \bar{\rho}), \tag{2}$$

which are equivalent to the Schrödinger equation where the potential is the self-potential due to self-gravity, plus a non-linear *attractive* self-interaction term (see e.g. Chavanis 2018). ψ is the wavefunction that describes the dark matter, normalized so that the dark matter density is $\rho = |\psi|^2$. $\bar{\rho}$ is the local mean dark matter density, and the s-scattering length a_s quantifies the SI strength. It is related to axion symmetry-breaking scale f by

$$a_s = \frac{\hbar c^3 m}{32\pi f^2}. \tag{3}$$

Other studies follow the convention that $a_s < 0$ for attractive self-interactions, in which the right-hand side of equation (3) and the last term in equation (1) would be negated. Equations (1) and (2) with $a_s = 0$ are the Schrödinger–Poisson equations commonly used to simulate FDM in the absence of self-interactions. The $|\psi|^2$ term in equation (1) comes from a Taylor expansion of the non-relativistic limit of the instantonic axion potential equation (Peccei & Quinn 1977; Di Vecchia & Veneziano 1980; Witten 1980). In our simulations, the GPP equations evolve an initial mass distribution into a single isolated dark matter halo with a central soliton.

2.1 Generalized density profile

Following Lora & Magaña (2014), the GPP equations can be solved numerically by assuming that ψ is spherically symmetric,

$$\psi(r,t) = \mathrm{e}^{-i\gamma t/\hbar}\phi(r),$$

where $\phi(r)$ is a positive, decreasing profile of an FDM soliton. Substituting into equation (1) and rearranging yields

$$-\frac{\hbar^2}{2m}\frac{1}{r}\frac{\partial^2}{\partial r^2}(r\phi) = \gamma\phi - mV\phi + \frac{4\pi\hbar^2 a_\mathrm{s}}{m^2}\phi^3$$
$$\frac{1}{r}\frac{\partial^2}{\partial r^2}(rV) = 4\pi G\phi^2.$$

Introducing dimensionless variables,

$$\hat{\phi} = \frac{\sqrt{4\pi G}\hbar}{mc^2}\phi \quad \hat{V} = \frac{1}{c^2}V$$
$$\hat{r} = \frac{mc}{\hbar}r \quad \hat{t} = \frac{mc^2}{\hbar}t$$
$$\hat{\gamma} = \frac{1}{mc^2}\gamma \quad \hat{a}_\mathrm{s} = \frac{c^2}{Gm}a_\mathrm{s}$$

the GPP equations take a simpler form:

$$\frac{\mathrm{d}^2}{\mathrm{d}\hat{r}^2}(\hat{r}\hat{\phi}) = 2\hat{r}(\hat{V}-\hat{\gamma})\hat{\phi} - 2\hat{r}\hat{a}_\mathrm{s}\hat{\phi}^3 \tag{4}$$

$$\frac{\mathrm{d}^2}{\mathrm{d}\hat{r}^2}(\hat{r}\hat{V}) = \hat{r}\hat{\phi}^2. \tag{5}$$

For an FDM soliton, we impose $r = 0$ boundary conditions $\partial_r\hat{\phi} = 0$, $\partial_r\hat{V} = 0$, and $\hat{\phi} = \hat{\phi}_\mathrm{c}$. For chosen values of $\hat{\phi}_\mathrm{c}$ and $\hat{a}_\mathrm{s}$, there is a discrete number of $\hat{\gamma}$ values $\{\hat{\gamma}_0, \hat{\gamma}_1, \hat{\gamma}_2, \ldots\}$ for which the solutions converge as $r \to \infty$. Each $\hat{\gamma}_i$ corresponds to a solution $\hat{\phi}_i(r)$, which has i nodes. We are interested in the *ground state* solution $i = 0$, the unique solution with $\phi(r) > 0$ at all radii and finite total mass.

We want to solve for the density profile $\rho(r) = |\phi(r)|^2$ at various SI strengths in hopes of developing an approximate functional form. The dimensionless density profile differs from the physical profile by some factor ϕ_0/ϕ_c, where $\rho_0 = \phi_0^2$ is the physical central density of the FDM halo. The GPP equations admit a scaling relation that implies a family of solutions for any particular solution:

$$\{r, \phi, \rho, a_\mathrm{s}\} \to \{\epsilon^{-1}r, \epsilon^2\phi, \epsilon^4\rho, \epsilon^{-2}a_\mathrm{s}\}. \tag{6}$$

In particular, a_s is a scale-*dependent* quantity; however, the density profile fitting formula must ultimately be scale-*independent*. To create a suitable self-interaction strength parameter, let $\hat{\phi}_\mathrm{c} = 1$ and $\epsilon = \phi_0/\phi_\mathrm{c}$. Define the scale-free parameter β as

$$\beta \equiv \epsilon^2\hat{a}_\mathrm{s} = \frac{\sqrt{4\pi G}\hbar}{mc^2}\rho_0^{1/2}\frac{c^2}{Gm}a_\mathrm{s}. \tag{7}$$

In terms of f and fiducial values,

$$\beta = 0.238\left(\frac{\rho_0}{10^{10}\ \mathrm{M_\odot kpc^{-3}}}\right)^{1/2} m_{22}^{-1} f_{15}^{-2} \tag{8}$$

where $m_{22} = m/(10^{-22}\,\mathrm{eV})$ and $f_{15} = f/(10^{15}\,\mathrm{GeV})$. This measure of SI strength is somewhat arbitrary (in the sense that we could have chosen any $\hat{\phi}_\mathrm{c}$), but can be conceptualized as the dimensionless s-scattering length $\hat{a}_\mathrm{s}$, scaled according to equation (6) from the physical central density ρ_0 to $\hat{\phi}_\mathrm{c} = 1$.

In the non-interacting case ($a_\mathrm{s} = 0$), the density profile of a soliton is well-fit by the single-parameter formula

$$\rho_\mathrm{sol}(r) = \rho_0\left[1 + 0.091\left(\frac{r}{r_\mathrm{c}}\right)^2\right]^{-8} \tag{9}$$

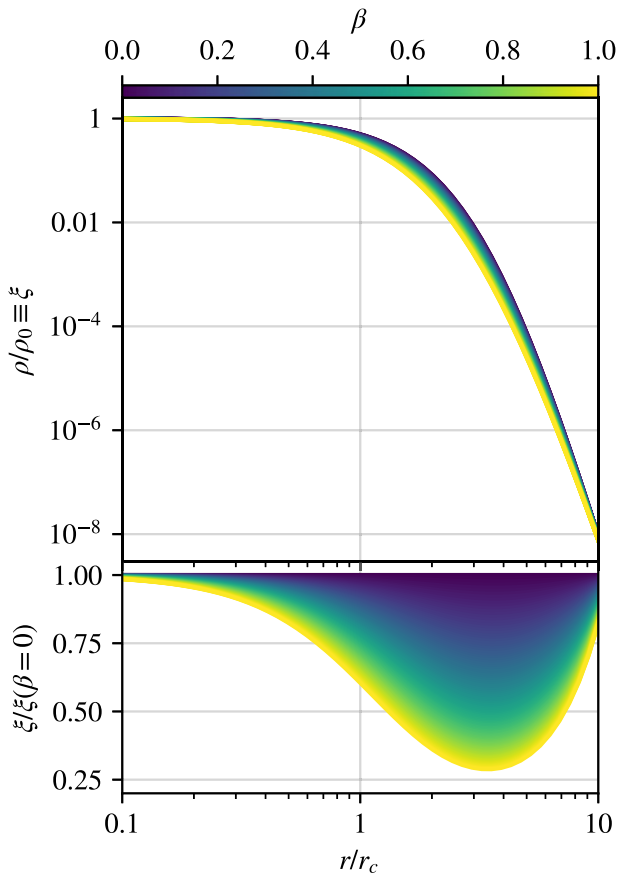

Figure 1. Upper: Density profiles of FDM solitons with attractive self-interactions of varying strengths, normalized by the central density and core radius, as given by equation (11). Self-interactions tend to shallow out the profile shape relative to the non-interacting case, decreasing the density at all radii within $r \lesssim 10\,r_\mathrm{c}$. Lower: The fractional change in the density profile relative to the non-interacting case $\beta = 0$. The greatest fractional decreases in density occur around $r \sim 3.5\,r_\mathrm{c}$.

(Schive et al. 2014a), where the core radius r_c is related to the central density ρ_0 by

$$\rho_0 = 1.9\times10^7\, m_{22}^{-2}\left(\frac{\mathrm{kpc}}{r_\mathrm{c}}\right)^4\frac{\mathrm{M_\odot}}{\mathrm{kpc^3}}. \tag{10}$$

In the general case ($a_\mathrm{s} \neq 0$), we find that the ground state solutions of equation (1) are well-fit by a simple one-parameter extension to equation (9),

$$\rho_\mathrm{sol}(r) = \rho_0\left[1 + 0.091\,a^2\left(\frac{r}{ar_\mathrm{c}}\right)^{2-\beta/b}\right]^{-8} \tag{11}$$

where $a = 11.2$ and $b = 4.2$ are best-fit constants to numerical solutions. Fig. 1 plots how equation (11) predicts that the soliton profile will change with β, relative to the non-interacting case $\beta = 0$. Based on this theoretical analysis, solitons with the same central density but stronger attractive self-interactions are expected to have *shallower* density profiles, with matter redistributed out of the interior and toward the outskirts. This fitting formula is restricted in domain to $\beta < 2\,b$, but the SI strengths in this study are all well within this threshold. In fact, as we will show in Section 2.2, solitons are likely to become unstable well before approaching $\beta = 2\,b$. We validate the accuracy of equation (11) over the relevant range of SI strengths

in Appendix A. See appendix C of Chen et al. (2021) for another general soliton fitting formula.

The self-interaction strength adds an additional degree of freedom to the soliton density profile, but in a physical model, it is a set universal constant (like the boson mass), while the central density parameter ρ_0 varies from halo to halo. In other words, after a_s and m parametrize the axion-like particle, ρ_0 characterizes the individual halo. So, a_s will vary between our simulations, but once it is set, ρ_0 is the only free parameter in equation (11).

2.2 Critical mass

Solitons under weak or zero self-interactions appear in a 'dilute' phase (Chavanis & Delfini 2011), in which they are well described by equation (11). However, axion self-interactions introduce a critical mass threshold for FDM solitons (Chavanis 2011; Chavanis & Delfini 2011; Chavanis 2016, 2018) that has been confirmed and studied in simulations (e.g. Levkov, Panin & Tkachev 2017; Chen et al. 2021; Glennon & Prescod-Weinstein 2021; Jain, Wanichwecharungruang & Thomas 2024),

$$M_{\rm crit} = \frac{1.012\hbar}{\sqrt{G m a_s}} \tag{12}$$

$$= 1.1\times10^9\,\frac{f_{15}}{m_{22}}\,{\rm M}_\odot. \tag{13}$$

If the mass of a soliton exceeds $M_{\rm crit}$, attractive self-interactions and gravity overcome the quantum pressure, leading to a rapid collapse. The end state of a collapsing soliton has been studied extensively in recent years. In a fully general relativistic treatment under spherical symmetry, Helfer et al. (2017) find that the end state depends on the assumed axion SI strength. If $f \gtrsim 0.4\,M_{\rm pl} \sim 10^{18}$ GeV, the critical mass is so high that the soliton remains dilute until its radius is comparable to its Schwarzschild radius, and the collapse leads to a black hole. Alternatively, if $f \lesssim 0.4\,M_{\rm pl}$, the collapse initiates an explosion, sometimes called a 'bosenova', accompanied by the ejection of relativistic axion shells until the remnant mass is lower than the critical mass (Levkov et al. 2017). The soliton is either completely dispersed or observed in its dilute state again. Using Taylor approximations of the instantonic axion potential, other studies have predicted the formation of 'compact' solitons supported by higher-order repulsive terms that are orders of magnitude smaller and denser than their dilute progenitors (Braaten, Mohapatra & Zhang 2016; Eby et al. 2016). However, it is unclear whether these structures are stable when the Taylor approximation and the non-relativistic assumption are relaxed (Visinelli et al. 2018).

In this study, we will only analyse solitons in their dilute states and in the early stages of collapse. Our fiducial values of SI strength ($f \sim 10^{15}$ GeV) ensure that dilute solitons remain well within the non-relativistic regime, so the GPP equations suffice to govern the evolution. For the early stages of collapse, we include the next higher-order term in the Taylor expansion of the axion cosine potential,

$$i\hbar\left(\frac{\partial}{\partial t}\right)\psi = \left(-\frac{\hbar^2}{2m}\nabla^2 + mV - \frac{4\pi\hbar^2 a_s}{m^2}\rho + \frac{32\pi\hbar^4 a_s^2}{3m^5c^2}\rho^2\right)\psi. \tag{14}$$

The new $\rho^2 = |\psi|^4$ term becomes non-negligible at very high densities, contributing a repulsive, stabilizing positive pressure,

$$P_4 = \frac{64\pi^2 a_s^2\hbar^4}{9m^6c^2}\rho^3. \tag{15}$$

This pressure will counterbalance the destabilizing pressure from the attractive term,

$$P_2 = -\frac{2\pi a_s\hbar^2}{m^3}\rho^2, \tag{16}$$

at a very high density,

$$\rho_{\rm eq} = \frac{9c^2m^3}{32a_s\hbar^2\pi}, \tag{17}$$

and above this density, P_4 dominates. With this two-term approximation of the full instantonic axion potential, compact solitons are the expected end state of collapse (Chavanis 2018). Braaten et al. (2016) makes analytic arguments that these two terms are a good approximation of the full cosine potential, but testing the approximation through all stages of collapse is left for future simulations. In this work, compact solitons are not resolved at the grid resolution.

We can define the regions of ρ_0–a_s parameter space, where the soliton is expected to be stable or unstable by integrating the density profile given by equation (11) to get a mass and comparing to equation (12). In the zero SI case, $\beta = 0$, the integral can be computed analytically,

$$M_{\rm sol} = \int_0^\infty 4\pi r^2\rho_{\rm sol}(r){\rm d}r \approx 11.6\rho_0 r_{\rm c}^3 \tag{18}$$

$$= 2.2\times10^8\left(\frac{10^{-22}\ {\rm eV}}{m}\right)^2\left(\frac{\rm kpc}{r_{\rm c}}\right){\rm M}_\odot \tag{19}$$

demonstrating the unique, well-studied property that more-massive FDM solitons are smaller. For other values of β, equation (11) can be integrated numerically. The left-hand panel of Fig. 2 shows a heat map of $M_{\rm sol}$ as a function of ρ_0 (or, equivalently, $r_{\rm c}$) and a_s (or f). Contours equally spaced in $\log\beta$ are shown as faded grey lines. For any constant value of ρ_0, stronger self-interactions *decrease* the soliton mass as compared to its non-interacting counterpart. Fixing a_s, increasing ρ_0 increases the soliton mass up to some maximum value before decreasing sharply. As shown in the right-hand panel, the soliton mass exceeds the critical mass through a range of central densities and peaks at $M_{\rm max} = 1.01M_{\rm crit}$, regardless of SI strength.

Using equation (11), the soliton mass formula can be easily extended from equation (18) with an additional multiplicative factor,

$$M_{\rm sol} = 11.6\,\rho_0 r_{\rm c}^3\,g(\beta), \tag{20}$$

where g is a smooth, monotonically decreasing function with $g(0) = 1$. We do not attempt to characterize $g(\beta)$ analytically, but we provide details in Appendix B. Dividing equation (20) by equation (12) and using the definition of β, it can be shown that the ratio of the soliton mass to the critical mass is simply a function of β,

$$\left(\frac{M_{\rm sol}}{M_{\rm crit}}\right)^2 = 3.8\,\beta g(\beta)^2 \tag{21}$$

Thus, the maximum of $M_{\rm sol}/M_{\rm crit}$ occurs at the maximum of $\beta g(\beta)^2$, which is determined to be approximately

$$\beta_{\rm max} = 0.687. \tag{22}$$

If the best-fit β were to surpass this value at some point in a simulation, the soliton mass as calculated by integrating equation (11) would start to *decrease*. More broadly, $M_{\rm sol} > M_{\rm crit}$ within the range $0.55 < \beta < 0.84$. In a simulated FDM soliton, β may slowly increase with ρ_0 and surpass the lower bound, $\beta_{\rm crit} = 0.55$, at which point it is expected to undergo the phase transition. This critical value

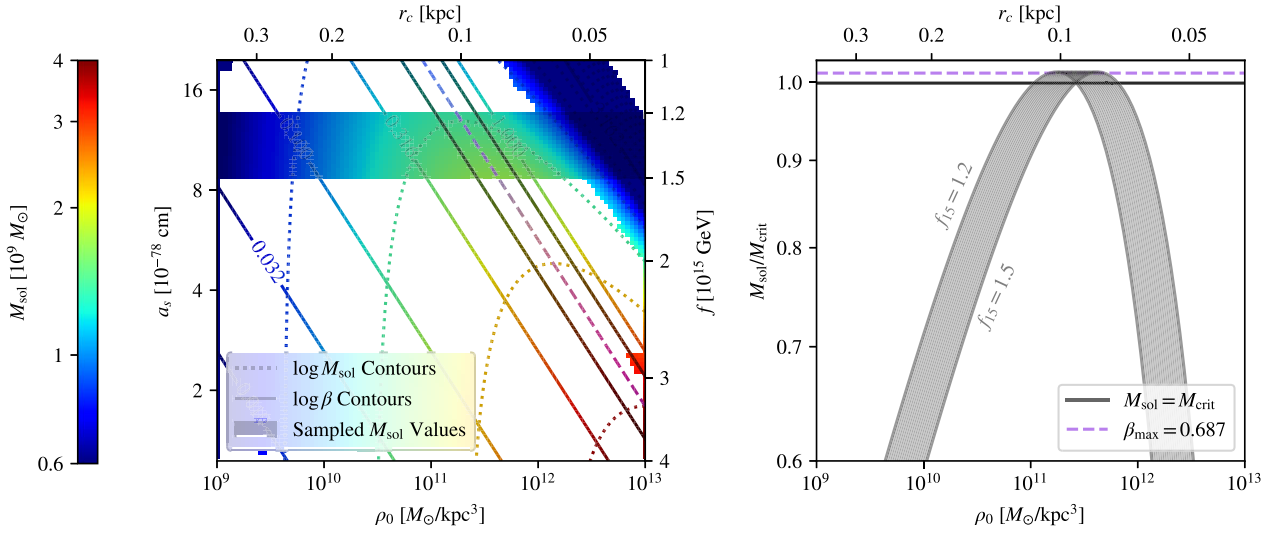

Figure 2. Left: Heatmap of soliton mass $M_{\rm sol}$ for a range of central densities ρ_0 and self-interaction strengths $a_{\rm s}$. Conversions to $r_{\rm c}$ and f are provided on the opposite axes. Overlaid are contours equally spaced in log $M_{\rm sol}$ (dotted curves) and contours equally spaced in log β (solid curves). The two contours bolded black ($\beta = 0.55, 0.84$) indicate $M_{\rm sol} = M_{\rm crit}$ and $\beta_{\rm max} = 0.687$ (purple dashed line) delineates the maximum predicted mass $M_{\rm max} = 1.01 M_{\rm crit}$ for any given $a_{\rm s}$. Right: $M_{\rm sol}$, normalized by the critical mass $M_{\rm crit}$, for every point in the shaded parameter space on the left-hand panel. Bounding curves are labelled by $f_{15} \equiv f/(10^{15}$ GeV). For any attractive SI strength, there exists a critical range of ρ_0 values in which the soliton is expected to collapse.

of β corresponds to a central density

$$\rho_{\rm crit} = 5.3 \times 10^{10}\, m_{22}^2 f_{15}^4 \,\frac{\rm M_\odot}{\rm kpc^3} \tag{23}$$

or a core radius

$$r_{\rm crit} = 0.138\, m_{22}^{-1} f_{15}^{-1}\,{\rm kpc}. \tag{24}$$

These values of $\beta_{\rm crit}$, $\rho_{\rm crit}$, and $r_{\rm crit}$ will serve as reference values in our simulation analysis.

2.3 Fitting algorithm

The density field of any simulation snapshot can be decomposed into a spherically-averaged radial profile about the soliton centre. For this work, we compute the density ρ at some radius r from the soliton centre – here defined as the densest point – by sampling the grid at a large number of points within a thin spherical shell $[r - \frac{\Delta r}{2}, r + \frac{\Delta r}{2}]$. Each point is assigned a sub-pixel coordinate value within the shell, and the density at that point is the density of the grid cell that encloses it. $\rho(r)$ is then the average of the density at all the sampled locations.

We are interested in measuring how self-interactions alter the distribution of matter in the entire FDM halo, including the soliton and the outer envelope. We choose to fit the whole profile simultaneously by assuming that $\rho(r)$ is the sum of two component profiles, $\rho_{\rm sol}(r)$ and $\rho_{\rm tail}(r)$, where $\rho_{\rm sol}$ is given in equation (11) and $\rho_{\rm tail}$ is defined as

$$\rho_{\rm tail}(r) \equiv \rho_{0,\rm tail}\left[1 + \left(\frac{r}{r_{\rm c,tail}}\right)^2\right]^{n_\infty/2} \tag{25}$$

and $\rho_{0,\rm tail}$, $r_{c,\rm tail}$, and n_∞ are all independent free parameters. At $r \gg r_{c,\rm tail}$, $\rho_{\rm tail}$ is approximately a power law with index n_∞. At small radii, the tail component flattens to avoid contributing to the soliton core. A transition radius $r_{\rm cutoff}$ can be defined as the radius at which $\rho_{\rm sol}(r)$ drops below $\rho_{\rm tail}(r)$ by half a dex. To correct for the slight curvature inherent in equation (25), we report the power-law slope at a radius $r_{\rm midtail}$ within the outer envelope,

$$n \equiv \frac{{\rm d}\log\rho_{\rm tail}}{{\rm d}\log r} = n_\infty \frac{(r/r_{c,\rm tail})^2}{1 + (r/r_{c,\rm tail})^2}\bigg|_{r=r_{\rm midtail}}, \tag{26}$$

where $r_{\rm midtail}$ is the log-mean of $r_{\rm cutoff}$ and $L/2$. In most snapshots, $n \approx n_\infty$.

In the full profile fit $\rho(r) = \rho_{\rm sol} + \rho_{\rm tail}$, there are four free parameters: $\rho_{0,\rm sol}$ from equation (11) (written there as ρ_0), $\rho_{0,\rm tail}$, $r_{\rm c,tail}$, and n_∞ from equation (25). Most important are the total central density $\rho_0 = \rho_{0,\rm sol} + \rho_{0,\rm tail}$ and the power-law index, n, from equation (26). We evaluate the goodness of fit using a sum of squares of differences metric,

$$\delta^2 = \frac{1}{J}\sum_j (\log\rho(r_j) - \log\rho_{\rm fit}(r_j))^2, \tag{27}$$

where J is the number of sampled density values. Since we can use this formula in any arbitrary radial interval, we evaluate an overall goodness of fit δ^2 as well as component evaluations $\delta^2_{\rm sol}$ and $\delta^2_{\rm tail}$.

2.4 Conservation of mass and energy

The system has conserved quantities, including its total mass,

$$M = \int \rho\, {\rm d}^3x, \tag{28}$$

and its total energy,

$$E = \int \frac{\hbar^2}{2m}(\nabla\sqrt{\rho})^2\, {\rm d}^3x + \int \frac{1}{2}\rho v^2\, {\rm d}^3x + \int \frac{1}{2}\rho V\, {\rm d}^3x \tag{29}$$

$$= K_\rho + K_v + W, \tag{30}$$

where K_ρ is the gradient energy due to the quantum pressure tensor, K_v is the classical kinetic energy, W is the potential energy, and $v = \arg(\psi)/m$ is the Madelung velocity. The total (quantum) kinetic energy is $K = K_\rho + K_v$. Like the density ρ, each of these energy components can be computed at every point in space and decomposed into a radial profile.

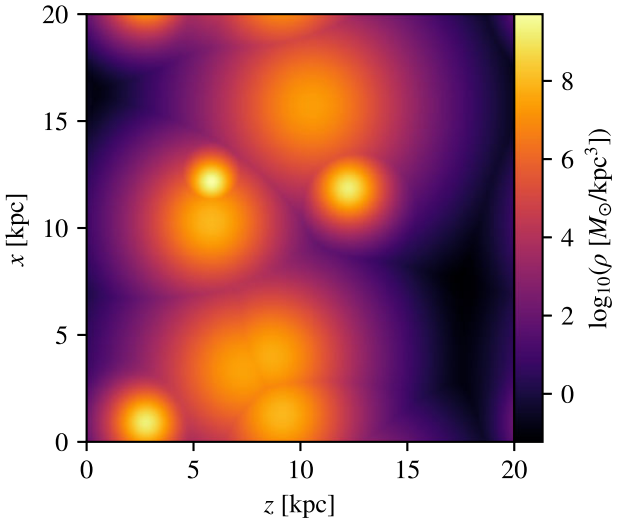

Figure 3. Density projection of the initial snapshot of our simulations, which is identical across all runs. Eight bare solitons are randomly strewn throughout the box with random masses drawn such that the total mass in the box is $M \sim 3 \times 10^9\,\mathrm{M}_\odot$. Box properties are listed in Table 1.

Table 1. Initial conditions in our simulation box, regardless of resolution or self-interaction parameter. A density projection of the initial box is shown in Fig. 3.

# of subhaloes	8
L	20 kpc
M	$3.65 \times 10^9 \mathrm{M}_\odot$
E	$-3.38 \times 10^{12} \mathrm{M}_\odot\,(\mathrm{km\,s^{-2}})$

3 IDEALIZED HALO SIMULATIONS

We numerically simulate the merging and evolution of self-interacting FDM haloes within a box with side length $L = 20\,\mathrm{kpc}$ and periodic boundary conditions. The only physical free parameter is the particle self-interaction strength, parametrized as $f_{15} \equiv f/(10^{15}\,\mathrm{GeV})$. We hold the dark matter particle mass fixed at its fiducial value of $m = 10^{-22}\,\mathrm{eV}$. Dark matter density is discretized onto grids with $N^3 = 200^3$ and 400^3 cells for uniform spatial resolutions of $\Delta x = 0.10$ and $0.05\,\mathrm{kpc}$. The initial conditions are non-cosmological and the dynamics do not include baryonic physics; the evolution is entirely described by equations (14) and (2). In future work, the code could be modified to include cosmological initial conditions, gas dynamics, and star formation, as in e.g. Mocz et al. (2020).

Our simulations are always initialized with the same density field, shown in Fig. 3. To create this field, we generated eight spherically symmetric bare solitons with density profiles given by equation (9) and core radii sampled from $r_\mathrm{c}/\mathrm{kpc} \sim U(0.2, 1)$. The subhaloes are initially unrealistic in the sense that they do not have outer envelopes, but the gravitational merging process is disruptive enough that the aftermath is not sensitive to this detail. We centred the haloes on randomly chosen locations in the $(20\,\mathrm{kpc})^3$ box, then we initialized the dark matter density ρ in an N^3 grid as the sum of contributions from all the haloes. The wavefunction ψ is initialized and normalized as $\psi = \sqrt{\rho}$, which is then subsequently evolved by equations (14) and (2). No angular momentum is imparted to the system. We provide some properties of the initial density field in Table 1.

The total mass in subhaloes is $M \sim 3 \times 10^9\,\mathrm{M}_\odot$, placing the merged halo in the mass range expected for haloes around dwarf galaxies. This halo mass is physically motivated and computationally advantageous. Dwarf galaxies are widely regarded as optimal testing grounds for constraining dark matter properties due to their large mass-to-light ratios (Bullock & Boylan-Kolchin 2017). Computationally, in FDM simulations, dwarf galaxy-mass haloes are less intensive to simulate because their solitons are more extended relative to those in higher-mass haloes (see, e.g. equation (19)).

We evolve the dark matter by numerically solving equations (14) and (2) following the spectral method as described in Mocz et al. (2017) and reviewed in Appendix B. For self-interacting FDM, a notable consequence of the spectral method is slow integration after solitons collapse. This is evident in equation (C7): if a soliton collapses into a very dense object, $\max|V|$ will grow very large, suppressing the time-step. However, as we will show in Section 4.2, artefacts of poor resolution render the post-collapse density fields unusable, so we do not spend large amounts of computational time in this regime.

In this work, our data consists of three suites of simulations detailed in Table 2. Our highest-resolution suite ($N^3 = 400^3$, $\Delta x = 0.05\,\mathrm{kpc}$) contains six simulations spanning a range of SI strengths between $f_{15} = \infty$ and 1.0. These simulations end at $T = 4\,\mathrm{Gyr}$ after the initial snapshot. In addition, we analyse two suites of lower-resolution ($N^3 = 200^3$, $\Delta x = 0.10\,\mathrm{kpc}$) simulations: the first, run to an end time of $T = 20\,\mathrm{Gyr}$, provides insight into the long-term evolution of the halo and the second explores trends and changes when SI strength is smoothly increased.

Snapshots of 400^3 complex wavefunction values, along with the simulation parameters and current time, are stored to disc every $\Delta t = 0.1\,\mathrm{Gyr}$. All relevant quantities can be derived from ψ.

Our choice of SI strengths is motivated by the critical threshold in equation (12) relative to the solitons in our dwarf galaxy-mass haloes. For a soliton of mass $M_\mathrm{sol} \sim 10^9\,\mathrm{M}_\odot$, SI strengths of $f \sim 10^{15}\,\mathrm{GeV}$ is expected to delineate the boundary between dilute and collapsed solitons. These self-interactions are 1 to 2 orders of magnitude stronger than those typically assumed in FDM cosmologies ($f \sim 0.5 \times 10^{17}\,\mathrm{GeV}$, Hui et al. 2017). In a cosmological simulation with $m = 10^{-22}\,\mathrm{eV}$ and such high SI strengths, the relic abundance of dark matter would be too small without fine-tuning the initial misalignment angle (Zhang & Chiueh 2017; Schive & Chiueh 2018; Hui 2021). However, our simulations are non-cosmological, and scaling symmetries in equation (6) ensure that our results can be rescaled to higher-mass haloes with weaker self-interactions.

Table 2. All simulations used in this paper, along with their purposes. For our initial conditions, the boundary between weak and strong interactions is between $f = 1.2$ and $1.1 \times 10^{15}\,\mathrm{GeV}$. In the third suite, f_{15} values are chosen to be evenly spaced in a_s.

#	f_{15}	N	Δx [kpc]	Δt [Gyr]	T [Gyr]	Purpose
6	$\{\infty, 2.0, 1.5, 1.2, 1.1, 1.0\}$	400	0.05	0.1	4	Highest-resolution simulations.
4	$\{\infty, 2.0, 1.5, 1.2\}$	200	0.10	0.1	20	Long-term evolution.
24	$\{\infty, 5.8, 4.1, \ldots, 1.2\}$	200	0.10	0.1	4	Quantifying trends with SI strength.

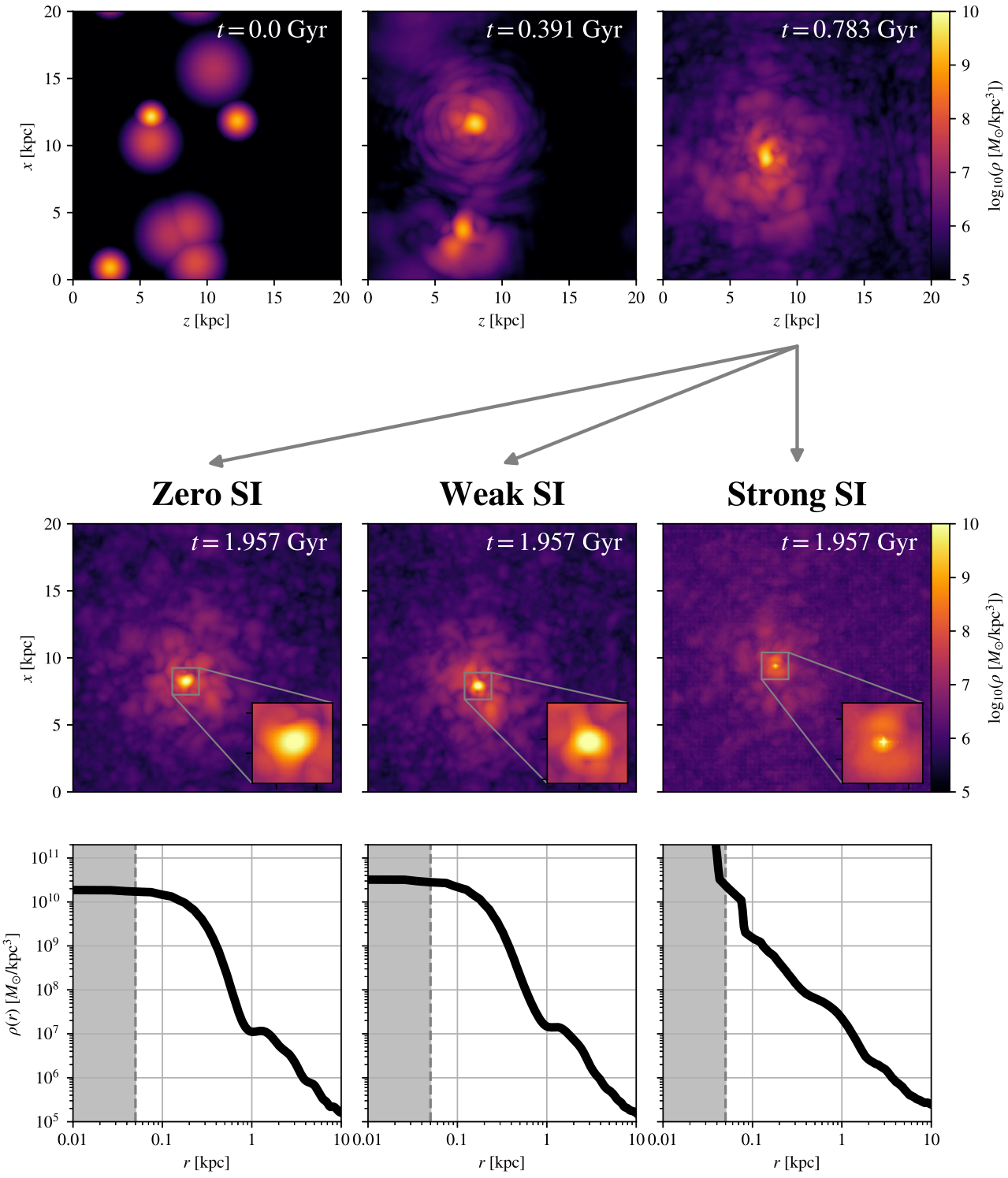

Figure 4. Evolution of haloes in our simulations. Initially, the subhaloes merge together in the same way (top panels), but the end state at ∼2 Gyr depends on the strength of the attractive SI. The simulations diverge once the subhaloes are fully merged and solitons condense in their centres (highlighted by the inset panels). As SI strength increases in the weak regime, the soliton becomes more compact while remaining in a dilute state. At some critical point that delineates the strong-SI regime, the self-interaction becomes strong enough to initiate a collapse into an unresolved compact soliton even though $M_{\rm sol} < M_{\rm crit}$.

4 RESULTS

Fig. 4 diagrams the general evolution of dark matter in our simulations. The top row of density projections depicts the early stages, before the subhaloes have fully merged together. The dynamics at these times are largely invariant of SI strength in the ranges we probed. In all cases, the subhaloes collide to produce a typical FDM halo with a soliton at its centre, NFW-like outer envelope, and turbulent 'granules' throughout the box. The simulations

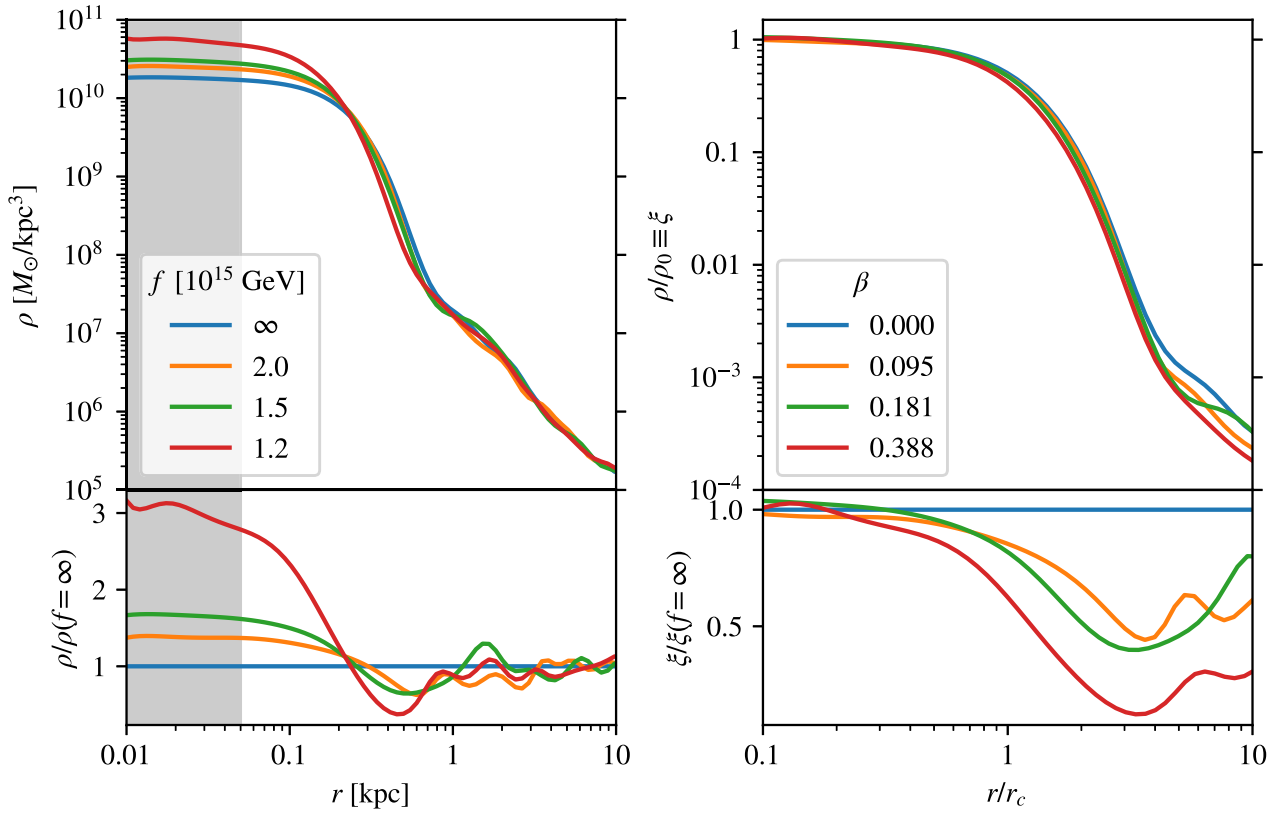

Figure 5. Left: Measured density profiles at the end of the $N = 400$, $f_{15} = \infty$ (blue), 2 (orange), 1.5 (green), and 1.2 (red) simulations. Stronger self-interactions increase the central density and decrease the core radius, making the soliton more compact. The outer envelope is not affected by self-interactions, except that it surrounds a smaller soliton. Right: Same profiles, normalized on both axes by r_c and ρ_0 (from best-fit models). The zero SI case is well fit by equation (9), but self-interactions introduce slight changes to the soliton shape that render equation (11) more accurate. Computed values of β are included for comparison to Fig. 1, which shows the theoretical prediction.

diverge after this point, represented by branches to three categories: non-interacting, weakly interacting, and strongly interacting cases.

In weakly interacting cases ($f_{15} = 2.0, 1.5, 1.2$), the soliton settles into a final state that depends on the interaction strength: stronger attractive interactions compactify the soliton to higher central densities and smaller radii. We examine dilute solitons in detail in Section 4.1.

In strongly interacting cases ($f_{15} = 1.1, 1.0$), the soliton collapses rapidly after some length of time that depends on the interaction strength. The uniform spatial resolution $\Delta x = 0.05$ kpc is not high enough to resolve the post-collapse remnants. Collapsed solitons appear as single high-density pixels that propagate numerical inaccuracies throughout the simulation box. The potential increases steeply at this time, and the time-step criterion in equation (C7) enforces that integration proceeds much more slowly. Since further evolution is inaccurate and computationally expensive, we halt these simulations shortly after collapse (before $T = 4$ Gyr). We analyse the frames immediately before and after collapse in Section 4.2.

4.1 Weakly self-interacting haloes

4.1.1 Density profiles

Density profiles of self-interacting FDM haloes with dilute solitons reproduce the key features of FDM haloes observed in previous simulations: a central soliton surrounded by a power-law tail. Fig. 5 plots the density profile measured at the end of the higher-resolution $f_{15} = \infty$ (blue), 2.0 (orange), 1.5 (green), and 1.2 (red) simulations. In each case, the soliton is clearly visible protruding within the central kiloparsec. It has a cored centre, with the density falling off at increasingly steep rates until some transition radius $r_{\rm cutoff}$. At $r > r_{\rm cutoff}$, the density profile assumes an NFW-like power-law shape with some fluctuations due to random interference granules. All self-interacting FDM haloes with dilute solitons demonstrate these properties in our simulations.

Fig. 5 reveals that, by the end of the simulations, self-interactions have caused multiple changes to the shape of the central soliton. The left-hand panel clearly suggests an important trend: *stronger* self-interactions make the soliton *more compact*. In other words, as we decrease f_{15}, we observe that the central density increases and the core radius shrinks. This makes intuitive sense: the soliton is the densest part of the halo in which the most particle-particle interactions will occur. Since that interaction is attractive, the soliton should compress into itself more. The degree of compression should be directly related to the SI strength, and this is reflected by the fact that the central densities are (inversely) sorted by f_{15}. By contrast, the outer envelope is unchanged by self-interactions; it has the same slope and amplitude at all radii exterior to $r_{\rm cutoff}$. For the smaller solitons in the self-interacting cases, the power law extrapolates inward to a new, smaller cutoff radius.

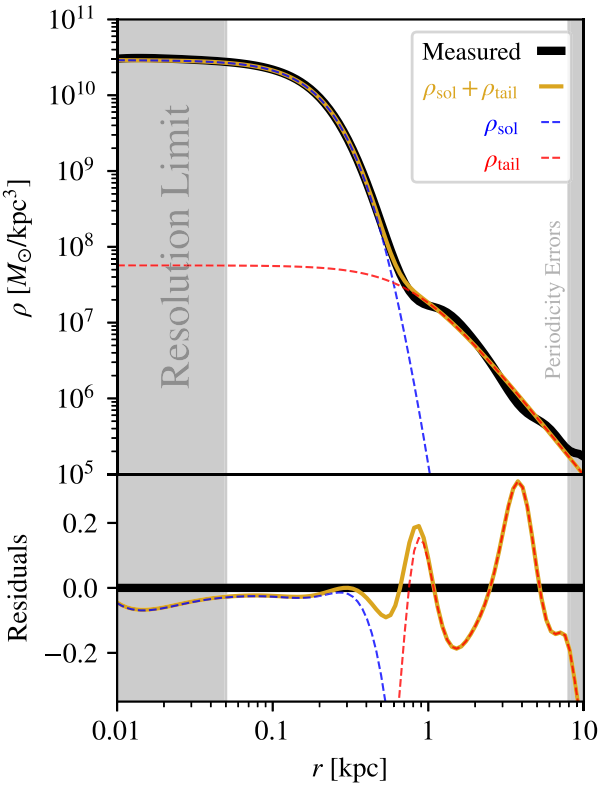

Figure 6. Upper: Example density profile measured from the $f_{15} = 1.5$ simulation (thick black curve) performed at the highest resolution, with best-fit model (gold curve) and fit components (red and blue-dashed curves). The region interior to the grid cell length $\Delta x = 0.05$ kpc is shaded in grey; regions beyond $\sim 0.4\,L = 8$ kpc are subject to periodicity errors. Equation (11) fits the soliton profile very well, while the outer envelope is roughly a power law with turbulent fluctuations. Lower: Ratio of best-fit components to the measured profile.

For the most part, the soliton shapes all resemble the zero-interaction case, but by normalizing ρ by the central density ρ_0 and r by the core radius r_c, as shown in the right-hand panel, the minute variations from equation (9) are exposed. For a given ρ_0, the density of self-interacting solitons falls off slightly faster than is allowed by equation (9), to the point that the $f_{15} = 1.2$ soliton has 1/4 the 'expected' density near the cutoff radius. Fitting equation (9) to the soliton component of the red curve yields a relatively poor goodness-of-fit value of $\delta^2 = 0.0571$, while equation (11) successfully predicts these minute changes, boasting a best-fit $\delta^2 = 0.0054$. As mentioned in Section 2.1, both of these formulas have only one free parameter.

Fig. 6 isolates one of the density profiles in Fig. 5 ($f_{15} = 1.5$, the green curve) and includes the theoretical best fit as computed by the algorithm in Section 2.3. The soliton and tail components of the fit are shown in red and blue, and their sum is plotted in gold. The log residuals are shown in the bottom panel. The soliton is fit very well by equation (11), with goodness of fit $\delta^2_{sol} = 0.0085$. The (approximate) power law is a good fit for the tail, though natural random fluctuations increase the residuals to $\delta^2_{tail} = 0.024$. All other snapshots of haloes with dilute solitons exhibit similarly excellent fits.

4.1.2 Halo evolution

The density profile fitting algorithm exemplified in Fig. 6 can be applied to all snapshots outputted throughout each simulation to measure the essential halo quantities over time. Fig. 7 shows the evolution of ρ_0, n, r_{cutoff}, and δ^2 derived from density profile fits for each of the higher-resolution $f_{15} = \infty$, 2.0, 1.5, and 1.2 simulations. The initial subhaloes do not fully merge together until $t_{merge} \approx 0.7$ Gyr, indicated by a grey-shaded region, at which point an FDM halo forms with a dilute soliton and outer envelope.

The upper-left-hand panel of Fig. 7 shows that the soliton central densities sort themselves by f_{15} after $t \approx 1.5$ Gyr. This reflects observations of the raw density profiles in Fig. 5. Turbulence in the box means the evolution of ρ_0 is noisy, but in all cases, a power law $\rho_0 \propto t^\alpha$ increase is observed after t_{merge} for α between 0.17 and 0.43. Since M_{sol} is roughly proportional to $\rho_0^{1/4}$, M_{sol} also increases like a power law. This phenomenon is observed in other studies and may be interpreted as a slow accretion of the outer envelope over time (Chen et al. 2021; Dmitriev et al. 2024).

The upper-right-hand panel plots the best-fit power-law index to the density profile tail over time. Immediately after t_{merge}, the slope is $n \approx -3.0$, but over time it slowly shallows to $n \approx -2.4$ by $t = 4$, independent of the SI strength. The 'shallowing' of the outer envelope is a response to mass accretion onto the soliton; matter is redistributing from the outer halo to the inner halo over time.

In the lower-left-hand panel, r_{cutoff} stabilizes after t_{merge} at a radius dependent on f_{15}. In fact, r_{cutoff}/r_c is invariant of f_{15}, so r_{cutoff} and r_c scale with interaction strength in the same way. Whereas the core radius decreases over time (since it is inversely related to ρ_0), the cut-off radius is observed to stay roughly constant. Thus, later in its evolution, the soliton extends out to higher multiples of r_c. This interesting phenomenon is the sum of the two effects in the upper panels: the soliton becomes more compact as it accretes more mass, but the outer envelope becomes shallower and lower amplitude such that the cutoff radius remains roughly the same.

In the lower-right-hand panel, the goodness of fit metric δ^2 is shown to be consistently low, independent of f_{15}. Further, the fits seem to get slightly better over the course of the simulation. This provides evidence that our $\rho_{sol} + \rho_{tail}$ fitting algorithm, particularly equation (11), is a good generalization of previous density profile approximations of FDM haloes.

To verify the power law increase of ρ_0 and the corresponding shallowing of the outer envelope observed in Fig. 7, we analyse a suite of four analogous simulations at an intermediate resolution $N = 200$ evolved to a much later $T = 20$ Gyr. Fig. 8 shows the results of these simulations in the same format as the top panels of Fig. 7. The simple moving averages are highlighted to isolate secular trends and reduce noise, and 4 Gyr is marked with a vertical line to indicate the end of the higher-resolution runs. Notably, a collapse is observed in the $f_{15} = 1.2$ simulation at $t = 5.87$ Gyr; this is discussed further in Section 4.2. For the others, the general increase of ρ_0 and n extends to the simulation end at 20 Gyr. The time dependence $\rho_0(t)$ is still well fit by a single power law t^α and $n(t)$ never levels out. This suggests that an equilibrium state is not reached, but rather the entire halo will be consumed in the asymptotic future. The dependence of ρ_0 and n on SI strength echoes Fig. 7: the central density clearly depends on interaction strength while the power-law index of the outer envelope does not.

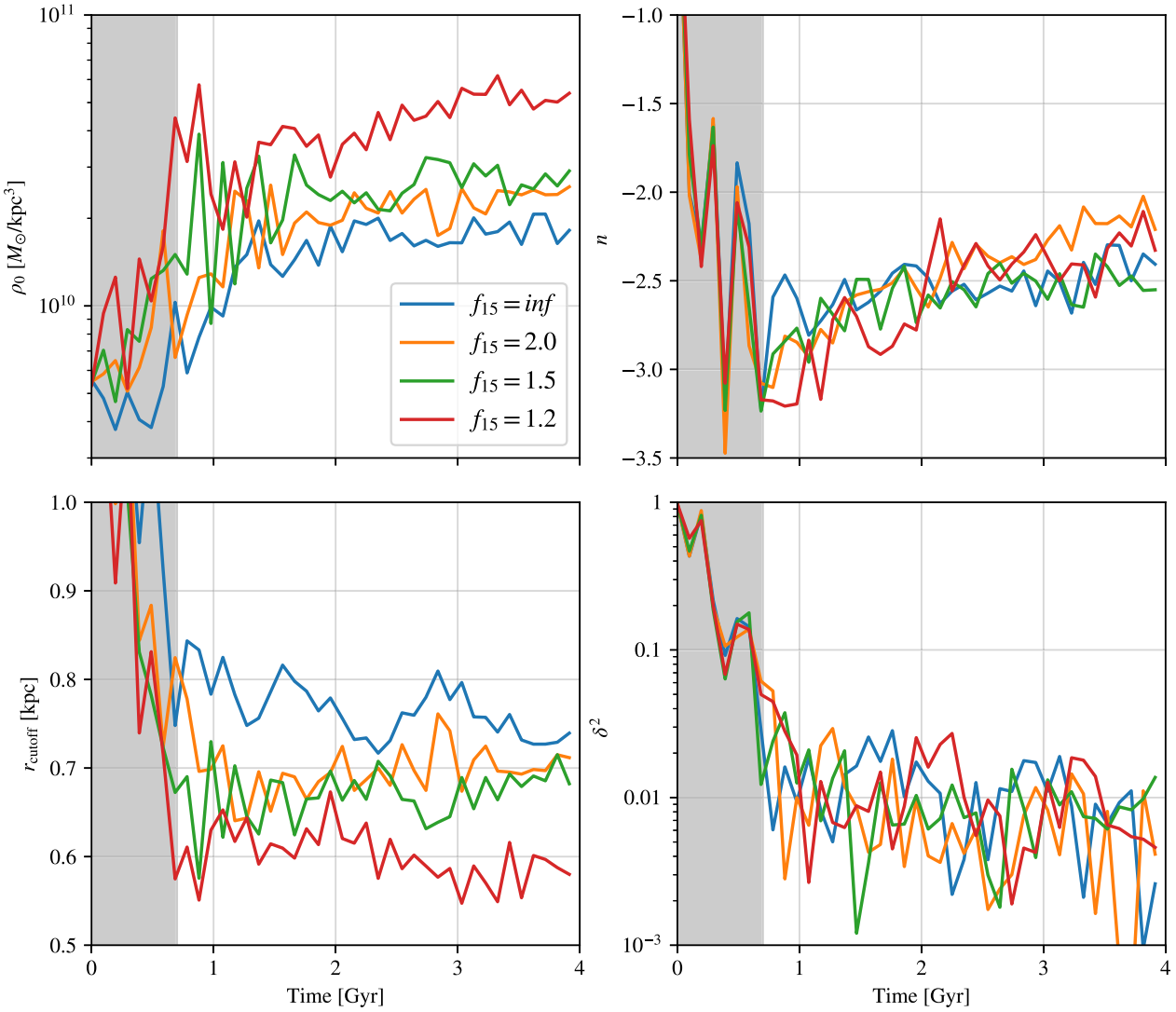

Figure 7. Best-fit quantities over time for weakly self-interacting FDM haloes. The time before all subhaloes have fully merged is indicated by the shaded area. Upper left: The soliton central density ρ_0 exhibits a clear pattern across the four SI strengths by $t \approx 1.5$ Gyr. Stronger self-interactions increase ρ_0 and thus decrease r_c. Upper right: The power-law index n of the outer envelope is independent of f_{15} and increases slowly over the course of the simulation. Lower left: The soliton cutoff radius $r_{\rm cutoff}$ decreases with stronger self-interactions, scaling in the same way as r_c. Lower right: The goodness of fit does not depend on f_{15}, oscillating around $\delta^2 = 10^{-2}$. Our fitting algorithm therefore appears to be valid across the weak SI regime.

4.1.3 Trends with self-interaction strength

Figs 5, 7, and 8 suggest that weakly attractive self-interactions smoothly change soliton properties. To see these changes more clearly, we extract and fit density profiles from our suite of 24 intermediate-resolution simulations spanning the weak SI regime. We continue to hold the initial configuration constant among each simulation; the only difference is the strength of self-interactions.

To be clear, the way in which the soliton density profile changes with ρ_0 and a_s is already accurately quantified in equation (11). What we hope to glean from these simulations is how ρ_0 changes with a_s for a fixed initial mass configuration. For our initial conditions, a_s parametrizes a particular curve $\rho_0(a_s)$ that traces a slice of $M_{\rm sol}$ or β heatmaps. In this sense, $M_{\rm sol}$ and β may be considered solely functions of a_s for our simulation setup, since ρ_0 is determined at every a_s (i.e. $M_{\rm sol}(a_s) \equiv M_{\rm sol}(\rho_0(a_s), a_s)$). However, if our simulation had different initial conditions, the relationship $\rho_0(a_s)$ would be different, and thus $M_{\rm sol}(a_s)$ and $\beta(a_s)$ would look different.

The left-hand panel of Fig. 9 plots ρ_0, the one free parameter in the fit to the soliton density profile, as measured at the end of each of these 24 simulations, as well as the four higher-resolution simulations introduced in previous subsections. The central density is sampled in each simulation from a density profile averaged over three consecutive snapshots to mitigate random fluctuations. The measurements confirm the trends suggested in previous figures: as compared to the collisionless case, ρ_0 increases smoothly with stronger self-interactions (and the core radius decreases according to equation (10)). The trend is not linear in ρ_0 or log ρ_0 but more closely resembles an asymptotic or exponential increase. Near the critical SI strength at which our soliton collapses ($f_{15} \sim 1.1$–1.2), the central density is approximately 3 times greater than in the non-interacting case.

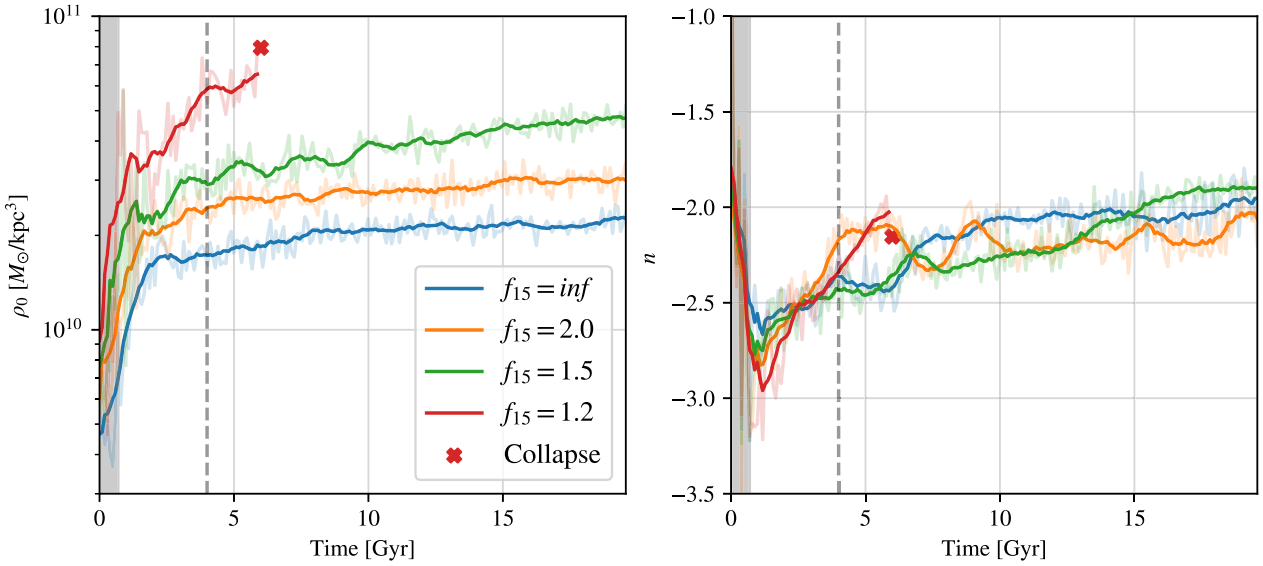

Figure 8. Extended evolution of the haloes in Fig. 7 using lower-resolution simulations ($N = 200$). These simulations reproduce the trends observed through the first 4 Gyr in Fig. 7 and continue them for an additional 16 Gyr. The soliton in the $f_{15} = 1.2$ simulation is observed to collapse at $t = 5.87$ Gyr, when it reaches its highest-yet central density of $\rho_0 = 8.03 \times 10^{10}\,\mathrm{M}_\odot\,\mathrm{kpc}^{-3}$. In the $f_{15} = \infty$, 2, and 1.5 simulations, both ρ_0 and n continue their secular increase over long time-scales, potentially reaching an equilibrium state in each case.

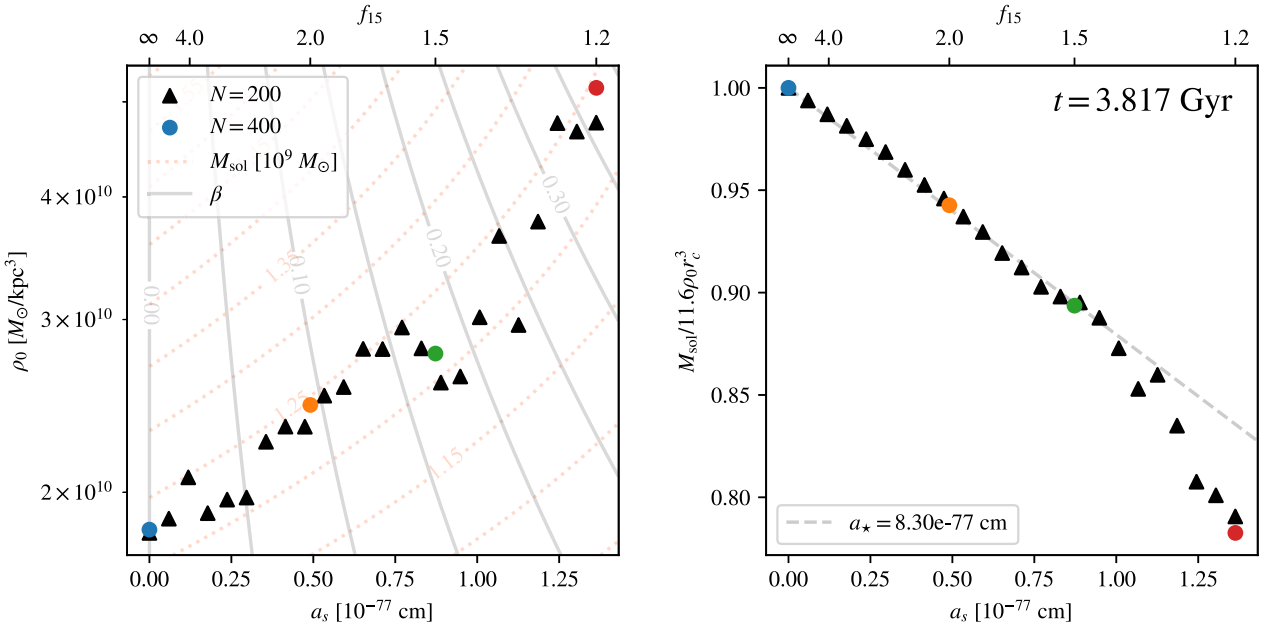

Figure 9. Soliton central density and mass (normalized) measured at $t = 3.817$ Gyr in simulations with various SI strengths and spatial resolutions. Included are $N = 400$ simulations (circles, same colours as previous figures) and our $N = 200$ suite (black triangles) evenly spaced in a_s. All simulations have the same initial conditions. Left: The central density smoothly increases with stronger self-interactions, as suggested by the snapshots in, e.g. Fig. 5. The trend steepens as the interaction strength nears the critical point at which the soliton collapses. At $f_{15} = 1.2$, ρ_0 is approximately 3 times higher than in the non-interacting case. The solid grey contours show constant values of β while the red dashed contours show constant values of $M_{\rm sol}$. β increases quickly with SI strength, but $M_{\rm sol}$ stays approximately constant. Right: Soliton mass, normalized by the prediction from equation (18). The residual dependence on a_s is roughly linear up until $f_{15} \approx 1.5$, at which point the decrease steepens, presumably because the soliton is nearing its critical point.

Overlaid are contours of equal β and contours of equal log $M_{\rm sol}$. As interaction strength increases, β increases quickly since both multiplicative terms in equation (8) are increasing. The changes to $M_{\rm sol}$ are a bit more complicated. From numerical integrals of equation (11), we know that increasing $a_{\rm s}$ generally decreases the soliton mass (see shape changes in the right-hand panel of Fig. 5), while increasing ρ_0 increases $M_{\rm sol}$ (typical $M_{\rm sol} \propto \rho_0^{1/4}$ growth in FDM haloes). In our simulations, ρ_0 increases in response to an increase in $a_{\rm s}$, so the resulting soliton mass is a product of two competing effects. We find that self-interactions increase ρ_0 in such a way that $M_{\rm sol}$ is nearly constant over our range of simulations, increasing only slightly from 1.20 to 1.25 $\times$ 10^9 $M_\odot$.

To isolate the deviations from the typical ρ_0–$M_{\rm sol}$ relation predicted by equation (18), we can normalize the measured $M_{\rm sol}$ at each $a_{\rm s}$ by the zero-SI prediction $M_{\rm sol}(a_{\rm s}=0) = 11.6\rho_0 r_{\rm c}^3$. The right-hand panel of Fig. 9 unveils a tight residual linear dependence of $M_{\rm sol}$ on $a_{\rm s}$ up to $f_{15} = 1.5$. This suggests that for very weak self-interactions (such that $M_{\rm sol} \ll M_{\rm crit}$), the soliton mass can be accurately predicted by revising equation (18) to

$$M_{\rm sol}(\rho_0, a_{\rm s}) = 11.6\rho_0 r_{\rm c}^3 \left(1 - \frac{a_{\rm s}}{a_\star}\right) \tag{31}$$

with one additional constant $a_\star$ characterizing the strength of the dependence. With our particular initial conditions, we find $a_\star \approx 8.30 \times 10^{-77}$ cm (which corresponds to $f_{15,\star} \approx 0.49$); the fit line with that slope is also plotted on the right-hand panel. Note that if equation (31) is true and $M_{\rm sol}$ is observed to remain roughly constant over a range of $a_{\rm s}$, then $\rho_0 \propto (1 - a_{\rm s}/a_\star)^{-4}$. After $f_{15} = 1.5$, the $a_{\rm s}$ dependence departs from linear. Presumably, this departure indicates that the soliton mass is nearing its critical mass and the higher-order ρ^2 term in equation (14) is no longer negligible.

4.1.4 *Energy profiles*

As with the density, the quantum gradient energy K_ρ, and classical kinetic energy K_v can be computed at each grid cell within the simulation box and may be decomposed into radial profiles. This analysis was considered in Mocz et al. (2017) and is useful for determining the energy composition of different regions of the halo and offers evidence as to the forces at play and the mechanisms driving the halo evolution.

Fig. 10 shows kinetic energy profiles at the end of our weakly self-interacting $N = 400$ simulations. The main features of the profiles are preserved regardless of f_{15}: mass and energy are most concentrated in the soliton with curves characteristic of FDM, and the curves fall off with power laws after a certain cutoff radius. However, the amplitude of each quantity at low radii is dependent on self-interactions. Stronger self-interactions enhance both kinetic energy components within the soliton core radius. In the left-hand panel, the K_v increases interior to $r \sim 0.5$ kpc when self-interactions are present, and the increase is sorted by SI strength interior to $r \sim 0.1$ kpc as in the density profiles. Similarly, in the right-hand panel, K_ρ is measured to increase interior to $r \sim 0.3$ kpc to some extent dependent on SI strength. In the $f_{15} = 1.2$ simulation, K_ρ is enhanced by more than an order of magnitude in the soliton centre. In both cases, the energy profile of the outer envelopes is invariant with interaction strength, further indicating that self-interactions are not prominent at these radii.

Both kinetic energy components maximize at $r \sim r_{\rm c}$ and decrease to a local minimum at the soliton centre, regardless of interaction strength.

4.2 Strongly self-interacting haloes

In Section 4.1, we analysed simulations with SI weak enough that the solitons remained dilute. However, we observe soliton collapses in three simulations with strong enough self-interactions. Two of these simulations are part of our higher-resolution $N = 400$ suite ($f_{15} = 1.1$ and 1.0), while the other is one of our extended lower-resolution runs ($f_{15} = 1.2$). In all of these simulations, the transition happens quickly ($\Delta t < 10$ Myr), and the collapse remnant is spatially unresolved ($r < 50$ pc), appearing as one single dense pixel. After the collapse, numerical artefacts of poor resolution are propagated throughout the box, reducing the credibility of the data on the outer envelope. However, we can analyse the frames immediately before and after the collapse event (Sections 4.2.1 and 4.2.2) and modify the physics to artificially resolve a compact soliton (Section 4.2.3).

4.2.1 *Phase transition*

Soliton collapse is readily apparent in density projections of the $f_{15} = 1.1$ and 1.0 simulations over a few select snapshots. Fig. 11 shows a sequence of three consecutive projections from the $f_{15} = 1.1$ simulation at our highest temporal resolution of $\Delta t = 10$ Myr. In the left-hand panel at $t = 1.22$ Gyr, the soliton is dilute, as it has been since the initial configuration fully merged at $t \approx 0.7$ Gyr. There are no unusual features in the halo that indicate an imminent collapse. Density profile fitting reveals that the soliton is well within the critical regime for $f_{15} = 1.1$: the central density is at its highest value yet ($\rho_0 = 1.85 \times 10^{11}$ $M_\odot$ kpc^{-3}) and the soliton mass is almost exactly equal to the critical mass ($M_{\rm sol} \approx M_{\rm crit} = 1.22 \times 10^9$ $M_\odot$). During the next 10 Myr (between the left and centre snapshots), the soliton collapses, but the collapse is halted when the soliton shrinks to the grid cell length. The remnant is displayed as a cross of five dense pixels in the centre panel. Spherical waves are observed to emanate from the centre at a velocity of $v \sim 10^3$ km s^{-1} with various frequencies. This radiation could be a physical signature of a 'bosenova', which has a characteristic spectrum as found by Levkov et al. (2017). However, the wavelengths are of order the grid cell length, so they are not fully converged. Higher resolution simulations are required to confirm whether these waves are physical or numerical artefacts of poor resolution. By $t = 1.24$ Gyr in the right-hand panel, the collapse remnant appears unphysically as one dense pixel surrounded by a small overdense cloud. The ripples have propagated through the periodic boundaries, distorting the granules and blurring vortex lines within the box (similar artefacts are observed by Jain et al. (2024), Appendix B). Neither the slope nor the amplitude of the power-law outer envelope changes during the collapse. Instead, the power law extends to fill the void left by the dilute soliton, leaving a cuspier halo profile. We stress that these results are not rigorous; simulations that adequately resolve the soliton collapse are required to thoroughly investigate the post-collapse halo structure.

With the two-term approximation of the instantonic axion potential, we expect that the collapse should result in a compact soliton wherein the higher-order repulsive pressure in equation (14) counterbalances the attractive SI and gravity. Equation (17) suggests that the post-collapse equilibrium density of the compact soliton should be $\rho_{\rm eq} \sim 3.7 \times 10^{17}$ $M_\odot$ kpc^{-3}, over six orders of magnitude higher than ρ_0, pre-collapse. Extrapolating the ρ_0-$r_{\rm c}$ relation in equation (10) to the post-collapse regime yields a compact radius of $r = 2.7$ pc, about 20 times finer than our best grid resolution. However, there is no evidence to suggest that equation (10) can

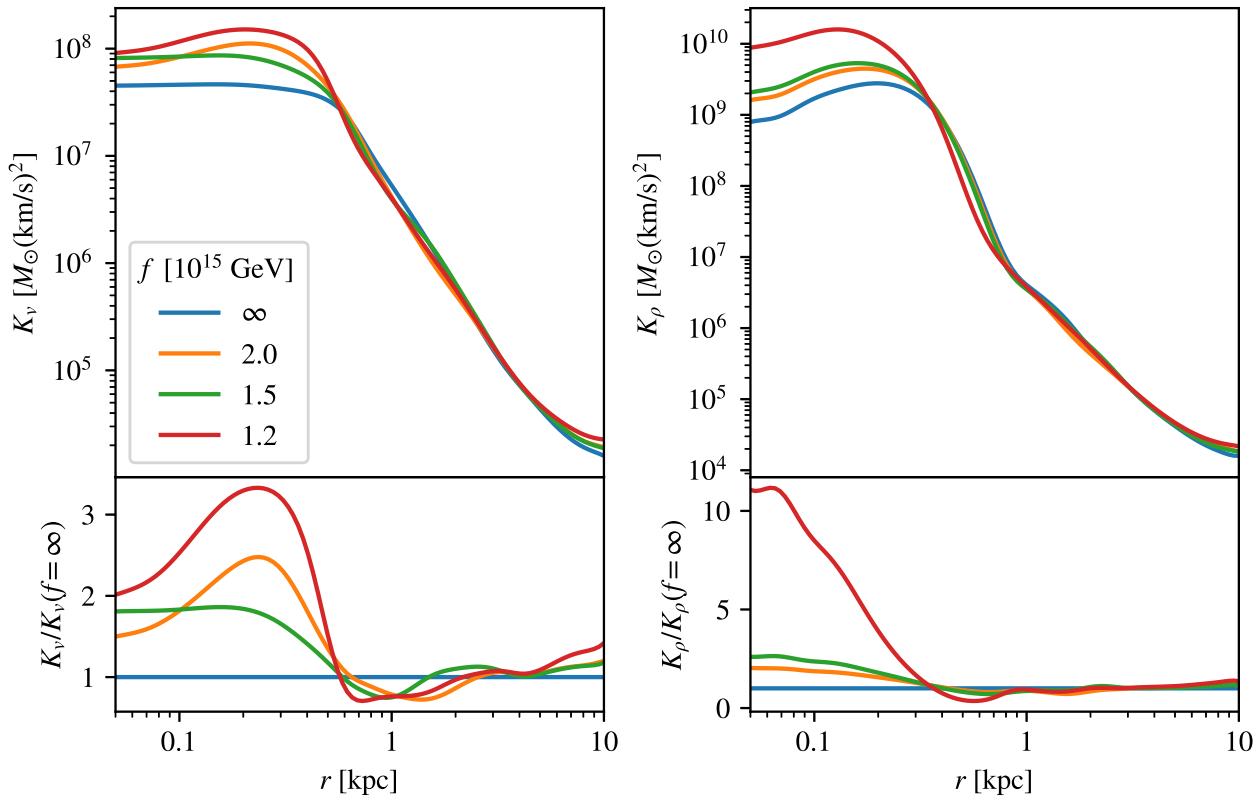

Figure 10. Classical kinetic energy K_v (left) and quantum gradient energy K_ρ (right) profiles at the end of each $N = 400$ simulation with weak self-interactions. Similar to the trends seen in the density profiles, stronger self-interactions enhance both components of the kinetic energy around the soliton with some degree of dependence on the interaction strength. In the outer envelope, the slope and amplitude of kinetic energy profiles are independent of self-interactions.

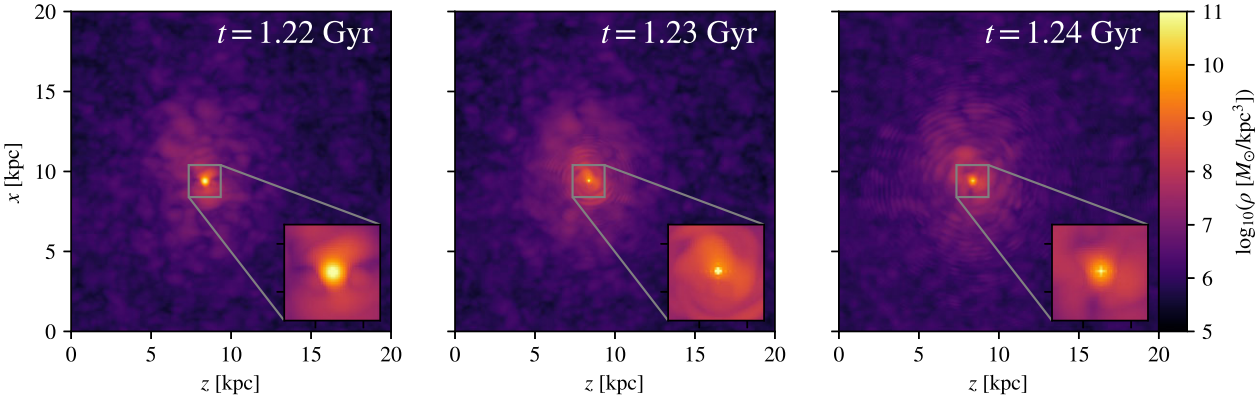

Figure 11. Soliton collapse under strong axion self-interactions ($f_{15} = 1.1$). Left: Just before collapsing, the soliton and outer envelope are typical of other snapshots of dilute solitons with no obvious indicators of an imminent collapse. Centre: Immediately after collapse, the soliton appears as a dense, tiny unresolved object with waves emanating from its centre. Right: Unphysical numerical artefacts from the unresolved soliton and collapse wavefronts blur and distort the outer envelope, rendering any post-collapse data unreliable.

be extrapolated in this way. If the mass of the compact soliton equals the mass of its dilute progenitor, and if the compact soliton can be approximated to a sphere of uniform density $\rho_{\rm eq}$, then the post-collapse radius is $r \sim (3M_{\rm sol}/4\pi\rho_{\rm eq})^{1/3} = 0.9$ pc. If matter is radiated during collapse, then this is an upper limit. These lengths are about four orders of magnitude higher than the Schwarzschild radius of the soliton $R_\bullet = 2GM_{\rm sol}/c^2 = 1.1 \times 10^{-4}$ pc, indicating that the higher-order $|\psi|^6$ repulsive pressure may halt the collapse before a black hole is formed.

Similarly, the free-fall time of the dilute soliton may give an order-of-magnitude estimate of the collapse time-scale. Using the pre-collapse central density, the free-fall time is $t_{\rm ff} \sim (G\rho_0)^{-1/2} = 1.2$ Myr, about 10 times finer temporal resolution than our smallest Δt between time-steps.

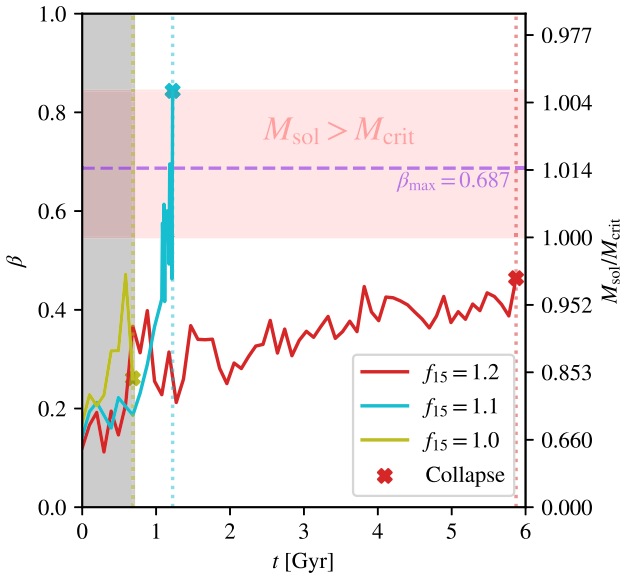

Figure 12. Stability parameter β tracked over time for each of the three simulations in which we observed a soliton collapse. In the red shaded region, $M_{sol} > M_{crit}$; the maximum M_{sol}/M_{crit} ratio is marked at $\beta_{max} = 0.687$, and the time period before all haloes fully merge together is shaded grey. The $f_{15} = 1.2$ soliton collapses at its highest-yet value of $\beta = 0.464$, where $M_{sol} \approx 0.97 M_{crit}$, after a gradual ∼5 Gyr increase. By contrast, the $f_{15} = 1.1$ soliton collapses right on the upper boundary of the $M_{sol} > M_{crit}$ region, at $\beta = 0.844$, after a steep ∼0.5 Gyr ascent. The $f_{15} = 1.0$ simulation collapses during the final major subhalo collision; finer time-steps would be needed to resolve the details.

Fig. 12 plots the dimensionless self-interaction parameter β, which is proportional to $\rho_0^{1/2}$, over time for each of the $f_{15} = 1.2$, 1.1, and 1.0 simulations up to the point of collapse. The grey shaded region indicates the period during which merging events take place and the × markings and vertical dotted lines indicate the moments right before each phase transition occurs. In this limited set of data, solitons collapsed first in simulations with stronger self-interactions. The $f_{15} = 1.0$ soliton collapsed during the last major merging event, before the dilute soliton had a chance to condense fully. The $f_{15} = 1.1$ soliton was dilute for a short period of ∼0.5 Gyr after merging was finished. The $f_{15} = 1.2$ soliton was dilute for much longer, slowly accreting mass for ∼5 Gyr before finally collapsing.

Notably, finer temporal sampling reveals that the central density in the $f_{15} = 1.1$ simulation increases immediately before collapse at an unusually fast pace. Whereas ρ_0 evolves slowly in other simulations with dilute solitons, in this case it violently oscillates up by a factor of ∼4 over <200 Myr from $t = 1.0$–1.2 Gyr. This stage of evolution is distinct from collapse, which happens much more quickly; the central density briefly accelerates while the soliton is still dilute before reaching some threshold for collapse. We did not perform finer sampling of the $f_{15} = 1.2$ simulation immediately before collapse; the time-steps remain at a default $\Delta t = 100$ Myr.

This data indicate only a very tight range of interaction strengths ($1.0 \lesssim f_{15} \lesssim 1.5$, for our halo mass) allows for a dilute soliton to form before collapsing at some point later in its lifetime. If f_{15} is higher, the soliton will remain dilute forever, but if f_{15} is lower, a collapse will occur before the soliton fully forms in a dilute state. Put differently, for a boson mass of $m \sim 10^{-22}$ eV and interaction strength near $f \sim 10^{15}$ GeV, the Universe would likely contain both dilute and compact solitons with collapses actively occurring as solitons accrete mass and surpass their critical threshold. If self-interactions are weaker, there may only be dilute solitons in the Universe, but if they are stronger, *every* halo may have undergone a collapse or multiple collapses.

4.2.2 *Threshold criteria for collapse*

The critical soliton mass in equation (12) offers a predictive threshold for soliton collapse, which we extended to other criteria in equations (22), (23), and (24) from numerical analysis of the ground state solution of the GPP equations. It is of interest to examine whether these criteria accurately predicted collapse in our simulations.

Fig. 12 includes corresponding M_{sol}/M_{crit} ratios on the right-hand axis, according to equation (21). The red-shaded region indicates the critical regime ($0.55 < \beta < 0.84$), where $M_{sol} > M_{crit}$, and the maximum predicted soliton mass is marked with a dashed purple line. The $f_{15} = 1.1$ and 1.2 simulations collapse on opposite sides of the critical regime at quite different values of β. The $f_{15} = 1.2$ soliton collapses after rising from $\beta \sim 0.3$ to 0.46 over 5 Gyr, reaching $M_{sol} \approx 0.97 M_{crit}$ but never quite surpassing the critical mass. We stress, however, that lower spatial resolution in this simulation may instigate soliton collapse prematurely and lower temporal resolution could mask late increases in central density. On the other hand, the $f_{15} = 1.1$ soliton ascends quickly through the critical regime to $\beta = 0.84$. Interestingly, the quick ascent triggers close to the lower $M_{sol} = M_{crit}$ boundary, and the collapse occurs right on the upper boundary. We conclude that the criteria given in equation (12) accurately predicts soliton collapse in our simulations to within a few per cent.

4.2.3 *Boosting the $|\psi|^6$ repulsive pressure*

To demonstrate the compact equilibrium into which the soliton may collapse with a resolution of $\Delta x = 0.05$ kpc, we artificially increase the higher-order stabilizing pressure term in equation (14) and rerun the $f_{15} = 1.1$ simulation with this change. This is completely unphysical; the relative coefficients of the first two terms in the Taylor expansion of the axion potential are determined by SI strength, boson mass, and the functional form of the potential. However, observing soliton collapse under similar physics can give useful intuition for behaviour in the real case.

Multiplying the higher order term by a 'boosting' factor $B \gg 1$ increases the repulsive pressure and halts collapse at a lower equilibrium density

$$\rho_{\text{eq, modified}} = \frac{\rho_{\text{eq}}}{B} \tag{32}$$

and thus, a larger compact soliton radius. In the $f_{15} = 1.1$ simulation, the dilute soliton is observed to have a central density of $\rho_0 \approx 1.85 \times 10^{11} \mathrm{M}_\odot\,\mathrm{kpc}^{-3}$, six orders of magnitude less than $\rho_{\text{eq}} \approx 3.7 \times 10^{17} \mathrm{M}_\odot\,\mathrm{kpc}^{-3}$. We find a boosting factor of $B = 10^5$ to be large enough to resolve the compact object while small enough that a collapse still initiates.

For direct comparison, we initialize a new simulation with the $t = 1.08$ Gyr snapshot from the default-physics $f_{15} = 1.1$ simulation. We evolve forward for 0.8 Gyr at a finer temporal resolution of $\Delta t = 10$ Myr.

Fig. 13 shows a sequence of density projections analogous to Fig. 11, but with the repulsive pressure boosted. The soliton remains dilute up through the $t = 1.43$ Gyr snapshot (left-hand panel; 0.21 Gyr later than with default physics) at which point the central density is $\rho_0 = 2.01 \times 10^{11}\ \mathrm{M}_\odot\,\mathrm{kpc}^{-3}$, the mass is $M_{sol} = 1.22 \times 10^9\ \mathrm{M}_\odot$ and $\beta = 0.88$. Relative to the default $f_{15} = 1.1$

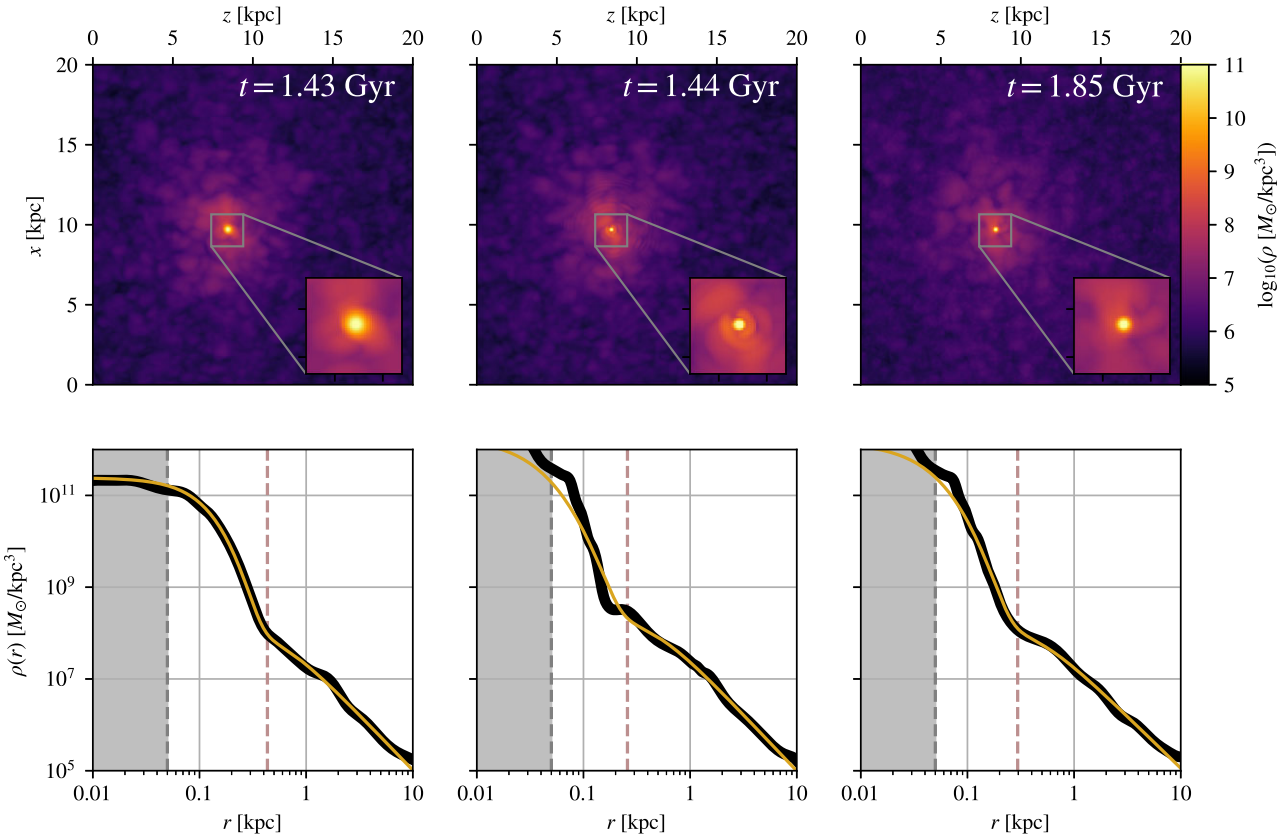

Figure 13. Top: Soliton phase transition under artificially modified physics that lowers the post-collapse equilibrium density by five orders of magnitude. In this modified regime, the compact soliton is resolved to have a diameter of ∼0.3 kpc, or about 6 pixels, and persists in a stable state through the end of the simulation. Bottom: The density profile of the compact soliton (thick black curves, centre and right) in this modified physics simulation is not as well-fit by the same fitting function (equation (11)) used for dilute solitons; the slope is too steep. However, the information is still very limited, and it is unclear how these results extrapolate to a fully collapsed object (with unmodified physics).

simulation, ρ_0 is slightly higher, presumably because the boosted higher-order pressure offers a slight additional resistance against collapse. The phase transition occurs quickly between $t = 1.43$ and 1.44 Gyr, leaving behind a compact soliton half the size of its dilute parent with an order of magnitude higher central density, $\rho_0 \approx 2.8 \times 10^{12}\ \mathrm{M_\odot\,kpc^{-3}}$. This is within a factor of two of the equilibrium density, $\rho_{\mathrm{eq,modified}} = 3.7 \times 10^{12}\ \mathrm{M_\odot\,kpc^{-3}}$ as calculated by equation (32). Waves of radiation similar to those observed in Fig. 11 are observed emanating from the compact object, suggesting that the radiation observed in Fig. 11 is physical. The soliton remains stably in its compact state for the remainder of the simulation. Density profiles are shown in the lower panels of Fig. 13; the dilute soliton fitting formula, equation (11), struggles to fit the steep slope of the compact soliton at $r = 0.08$–0.2 kpc. However, even in this modified regime, the information is very limited: the compact soliton is only resolved by ∼7 pixels in diameter. Furthermore, it is unclear how these results extrapolate to a fully collapsed object with unmodified physics. Ultimately, this test demonstrates that under very similar governing equations, the soliton collapses from a dilute state to a stable dense configuration, radiating matter waves in the process.

5 DISCUSSION

The simple one-parameter FDM model has likely been excluded as a dominant component of dark matter in the Universe because it is unable to reconcile extended cores in dwarf galaxy dark matter haloes with adequate structure observed in the Lyman-α forest. However, more general models of wave dark matter may offer the same benefits of FDM (e.g. fewer satellite galaxies, cored haloes, natural production in the early universe with the correct abundance) while boosting small-scale power. Attractive axion self-interactions are one such extension, offering a critical mass scale above which the inner part of the dark matter halo contracts and generates structure on smaller scales.

Although soliton collapse may be the key to generating small-scale structure in FDM models, many aspects of it remain unclear. In our simulations, we employ two standard approximations that are valid for dilute solitons: (1) the fully relativistic Klein–Gordon–Einstein (KGE) equations are approximated in the non-relativistic limit by the GPP equations, equations (14) and (2), and (2) the full instantonic axion potential ν is approximated by the first two terms in its Taylor expansion. Under these assumptions, the likely result of soliton collapse is a compact soliton, a stable, dense dark object wherein gravity and attractive SI are counterbalanced by the ρ^2 repulsive term in equation (14) (Chavanis 2018). Although Braaten et al. (2016) suggests that the two-term approximation accurately resembles $\mathcal{V}$, such objects have not been found in relativistic simulations with the full potential. In spherically-symmetric simulations, Helfer et al. (2017) finds that soliton collapses either disperse the soliton or form a black hole (in very massive haloes with very low SI strengths $f \gtrsim 10^{18}$ GeV). In similar simulations, Levkov et al. (2017) elaborates that soliton collapses emit waves of relativistic axions

with a characteristic spectrum. Our simulations provide evidence that such radiation is also emitted under our approximations. In future work, it will be interesting to fully resolve the radiation and compare it to that observed in relativistic simulations. In our simulations, the radiation interferes with itself through the periodic boundaries and distorts the vortex lines in the box (Jain et al. (2024) suggests that these effects will eventually homogenize the simulation box). If the ripples are physical, it may be necessary to simulate the outer envelope in high resolution to fully capture the post-collapse equilibrium configuration. We cannot study the effects of the radiation on the envelope here because, simultaneously, unphysical high-frequency modes propagate throughout the box from the unresolved collapse remnant. Post-collapse snapshots are thus highly distorted by multiple numerical artefacts.

Observationally, the prospects for constraining FDM self-interactions are limited to searching for the effects of soliton collapses. Weakly attractive self-interactions change the dilute soliton density profile only slightly: it becomes more compact but with a less extended core than predicted in the simple FDM model. Currently, rotation curves of nearby galaxies are not measured precisely enough to constrain the self-interaction parameter by discerning between density profiles; the change is too small and only present in the inner parsec of the halo (the outer NFW-like envelope is not affected by self-interactions).

For self-interactions strong enough to instigate soliton collapse, observational signatures may be present. From cosmological constraints, the axion decay constant is expected to be $f \sim 10^{17}\,\mathrm{GeV}$ (Hui 2021). In a model universe with this SI strength, solitons more massive than $M_{\rm sol} \sim 10^{11}\,\mathrm{M}_\odot$ (by equation (12)) are expected to have undergone at least one collapse event, corresponding to the haloes around the most massive galaxies and galaxy clusters. Less massive DM haloes, namely dwarf galaxies, would feature solitons in their dilute states. A slightly stronger (weaker) SI strength would lower (raise) the critical mass threshold. Soliton collapses have been proposed as possible seeds for supermassive black holes (e.g. Padilla et al. 2021) and the source of background axion radiation similar to gravitational wave backgrounds (e.g. Fox, Weiner & Xiao 2023).

In our simulations, we choose fiducial self-interaction strengths of $f \sim 10^{15}\,\mathrm{GeV}$, about two orders of magnitude stronger than the expected values. We do this to noticeably influence and initiate collapses in haloes of mass $M \sim 3 \times 10^9\,\mathrm{M}_\odot$, a computationally convenient mass scale because the solitons are relatively extended in the halo. However, our results can be generalized using scaling relations in equation (6) to higher-mass haloes with weaker SI strengths. In particular, $\{a_{\rm s}, M\} \rightarrow \{\epsilon^{-2}a_{\rm s}, \epsilon M\}$.

In our simulations, we observe the halo in snapshots before and during collapse. Based on pre-collapse soliton mass values, we find a rough agreement (within ∼3 per cent) with the critical mass formula, equation (12), developed in Chavanis (2011) and Chavanis & Delfini (2011). Equation (12) assumes a static, isolated initial condition and should be considered an approximation for our simulations.

Besides spatial and temporal resolution, our simulations are limited in that we test only one initial mass configuration. It would be interesting to confirm that higher or lower mass solitons still obey the generalized density profile, equation (11), and the critical mass formula, equation (12).

6 CONCLUSION

In this work, we investigate the structure of FDM haloes evolving under the GPP equations with a two-term Taylor approximation of the axion instantonic potential. We summarize the principal observations from our idealized simulations as follows:

(i) Attractive self-interactions introduce a critical mass threshold above which the central soliton collapses from its 'dilute' state. Our simulations suggest that a stable 'compact' soliton is the end state under our two-term Taylor approximation of the full potential, but fully relativistic studies suggest that these objects are unlikely to be stable. A soliton can either collapse at the time of formation or later in its life by accreting matter from the outer envelope and eventually exceeding the critical mass.

In the weak self-interaction regime:

(i) Solitons formed from identical initial conditions change shape to some degree dependent on the particle interaction strength. Stronger self-interactions *increase* the central density ρ_0 and *decrease* the core radius $r_{\rm c}$ relative to the collisionless case. The observed decrease in $r_{\rm c}$ very nearly follows the expected $r_{\rm c} \propto \rho_0^{-1/4}$ dependence in equation (10), but a slight correction is observed to be non-negligible (see Fig. 5).

(ii) We find that the soliton density profile is accurately generalized by the fitting formula in equation (11). This approximation is calibrated on numerical analysis of the ground state solution of the GPP equations and validated by our simulations.

(iii) The soliton mass $M_{\rm sol}$ is nearly constant as self-interactions are dialed up. Typical $M_{\rm sol} \propto \rho_0^{1/4}$ dependence is nearly counterbalanced by deviations in the density profile seen in the right-hand panel of Fig. 5. For very weak self-interactions ($f_{15} \geq 1.5$), $M_{\rm sol}$ can be approximated by equation (31), a generalization of equation (18) with a simple linear dependence on the s-scattering length.

(iv) The outer envelope of the halo that surrounds the soliton is invariant of SI strength. Evidence suggests this lack of dependence extends to the strong interaction regime, as neither the slope nor amplitude of the outer envelope density profile appears to change after a soliton phase transition.

(v) Solitons accrete matter from the outer envelope over time, growing as $\rho_0 \propto t^{\alpha}$. The logarithmic rate α positively correlates with SI strength: stronger SI yields faster growth. In response, the outer envelope becomes shallower and lower amplitude. Power law growth deviates into a runaway collapse when the critical mass is reached.

In the strong self-interaction regime:

(i) In our simulations, the collapse event is temporally unresolved ($\Delta t_{\rm collapse} < 10\,\mathrm{Myr}$) and the collapse remnant is spatially unresolved ($r < 50\,\mathrm{pc}$). Additional tests with modified physics indicate that the collapse will result in a compact soliton with central density close to the equilibrium density given in equation (17).

(ii) The time period during which a soliton is dilute before collapsing depends on interaction strength. If interactions are too weak, the soliton will never collapse. If interactions are too strong, as in our $f = 1.0 \times 10^{15}\,\mathrm{GeV}$ run, the dense centre will collapse before a dilute soliton has a chance to form. In a very tight range for us $1.0 \times 10^{15} \lesssim f \lesssim 1.5 \times 10^{15}\,\mathrm{GeV}$, a dilute soliton can form before later transitioning to its compact state.

(iii) Immediately before collapsing, a dilute soliton may undergo a runaway ascent in central density unlike the secular evolution observed when $M_{\rm sol}$ is significantly less than $M_{\rm crit}$ (see $f = 1.1 \times 10^{15}\,\mathrm{GeV}$ simulation in Fig. 12).

(iv) Soliton collapses in our simulations are accompanied by waves of axion radiation similar to that observed in fully relativistic simulations (Helfer et al. 2017; Levkov et al. 2017). It remains to

be verified that the characteristic spectrum of the radiation can be reproduced by non-relativistic simulations.

Naturally predicted axion-like self-interactions with a symmetry-breaking scale $f \sim 10^{17}$ GeV can significantly alter the predictions made from the simple FDM model. Every DM halo in the Universe above a certain critical mass would be expected to contain a remnant of soliton collapse, possibly in the form of a supermassive black hole, which could spawn strong non-linear effects on small scales and remedy the *Catch-22* that faces FDM. Lower-mass haloes are expected to retain dilute solitons, which smoothly approximate vanilla FDM solitons as $f \to \infty$. From here, the most important next step is to carefully simulate soliton collapse in three dimensions with full general relativistic effects to develop a seeding formula for cosmological simulations. With models for soliton phase transition and post-collapse interactions with the host haloes, large-scale simulations can determine whether attractive self-interactions broaden FDM parameter space enough to satisfy modern observations of both dwarf galaxies rotation curves and small-scale structure in the Lyman-α forest.

ACKNOWLEDGEMENTS

We thank David J. E. Marsh for a detailed and constructive report that helped us improve the content and clarity of the paper. CAP was partially supported by NSF grant AST-2108962. MBK acknowledges support from NSF CAREER award AST-1752913, NSF grants AST-1910346 and AST-2108962, NASA grant 80NSSC22K0827, and HST-AR-15809, HST-GO-15658, HST-GO-15901, HST-GO-15902, HST-AR-16159, HST-GO-16226, HST-GO-16686, HST-AR-17028, and HST-AR-17043 from the Space Telescope Science Institute, which is operated by AURA, Inc., under NASA contract NAS5-26555. PM acknowledges this work was in part performed under the auspices of the U.S. Department of Energy by Lawrence Livermore National Laboratory under contract DE-AC52-07NA27344, Lawrence Livermore National Security, LLC.

DATA AVAILABILITY

The data underlying this article will be shared on reasonable request to the corresponding author.

REFERENCES

Aghanim N. et al., 2020, A&A, 641, A6
Alam S. et al., 2021, Phys. Rev. D, 103, 083533
Amin M. A., Mocz P., 2019, Phys. Rev. D, 100, 063507
Amin M. A., Jain M., Karur R., Mocz P., 2022, J. Cosmol. Astropart. Phys., 2022, 014
Arvanitaki A., Dimopoulos S., Dubovsky S., Kaloper N., March-Russell J., 2010, Phys. Rev. D, 81, 123530
Arvanitaki A., Dimopoulos S., Galanis M., Lehner L., Thompson J. O., Van Tilburg K., 2020, Phys. Rev. D, 101, 083014
de Blok W. J. G., 2010, Adv. Astron., 2010, 789293
Boylan-Kolchin M., Bullock J. S., Kaplinghat M., 2011, MNRAS, 415, L40
Braaten E., Mohapatra A., Zhang H., 2016, Phys. Rev. Lett., 117, 121801
Bullock J. S., Boylan-Kolchin M., 2017, ARA&A, 55, 343
Burkert A., 2020, ApJ, 904, 161
Chavanis P.-H., 2011, Phys. Rev. D, 84, 043531
Chavanis P.-H., 2016, Phys. Rev. D, 94, 083007
Chavanis P.-H., 2018, Phys. Rev. D, 98, 023009
Chavanis P.-H., Delfini L., 2011, Phys. Rev. D, 84, 043532
Chen J., Du X., Lentz E. W., Marsh D. J., Niemeyer J. C., 2021, Phys. Rev. D, 104, 083022
Dalal N., Kravtsov A., 2022, Phys. Rev. D, 106, 063517
Davies E. Y., Mocz P., 2020, MNRAS, 492, 5721
Dawoodbhoy T., Shapiro P. R., Rindler-Daller T., 2021, MNRAS, 506, 2418
Del Popolo A., Le Delliou M., 2017, Galaxies, 5, 17
Desjacques V., Kehagias A., Riotto A., 2018, Phys. Rev. D, 97, 023529
Di Vecchia P., Veneziano G., 1980, Nucl. Phys. B, 171, 253
Dmitriev A. S., Levkov D. G., Panin A. G., Tkachev I. I., 2024, Phys. Rev. Lett., 132, 091001
Dome T., Fialkov A., Mocz P., Schäfer B. M., Boylan-Kolchin M., Vogelsberger M., 2023, MNRAS, 519, 4183
Dome T., Azhar R., Fialkov A., 2024, MNRAS, 527, 10397
Du X., Schwabe B., Niemeyer J. C., Bürger D., 2018, Phys. Rev. D, 97, 063507
Eby J., Leembruggen M., Suranyi P., Wijewardhana L. C. R., 2016, J. High Energy Phys., 2016, 66
Eby J., Leembruggen M., Street L., Suranyi P., Wijewardhana L. C. R., 2020, J. Cosmol. Astropart. Phys., 2020, 020
Elgamal S., Nori M., Macciò A. V., Baldi M., Waterval S., 2024, MNRAS, 532, 4050
Flores R. A., Primack J. R., 1994, The Astrophysical Journal, 427, L1
Foote H. R. et al., 2023, The Astrophysical Journal, 954, 163
Fox P. J., Weiner N., Xiao H., 2023, Phys. Rev. D, 108, 095043
Garrison-Kimmel S., Boylan-Kolchin M., Bullock J. S., Kirby E. N., 2014, MNRAS, 444, 222
Glennon N., Prescod-Weinstein C., 2021, Phys. Rev. D, 104, 083532
Guo H.-K., Sinha K., Sun C., Swaim J., Vagie D., 2021, J. Cosmol. Astropart. Phys., 2021, 028
Guzmán F., Ureña-López L., 2003, Phys. Rev. D, 68, 024023
Hayashi K., Ferreira E. G. M., Chan H. Y. J., 2021, ApJ, 912, L3
Helfer T., Marsh D. J. E., Clough K., Fairbairn M., Lim E. A., Becerril R., 2017, J. Cosmol. Astropart. Phys., 2017, 055
Hu W., Barkana R., Gruzinov A., 2000, Phys. Rev. Lett., 85, 1158
Huang H., Schive H.-Y., Chiueh T., 2023, MNRAS, 522, 515
Hui L., 2021, ARA&A, 59, 247
Hui L., Ostriker J. P., Tremaine S., Witten E., 2017, Phys. Rev. D, 95, 043541
Iršič V., Viel M., Haehnelt M. G., Bolton J. S., Becker G. D., 2017, Phys. Rev. Lett., 119, 031302
Jain M., Amin M. A., 2023, J. Cosmol. Astropart. Phys., 2023, 053
Jain M., Wanichwecharungruang W., Thomas J., 2024, Phys. Rev. D, 109, 016002
Klypin A., Kravtsov A. V., Valenzuela O., Prada F., 1999, ApJ, 522, 82
Kopp M., Vattis K., Skordis C., 2017, Phys. Rev. D, 96, 123532
Laguë A., Bond J. R., Hložek R., Marsh D. J. E., Söding L., 2021, MNRAS, 504, 2391
Laguë A., Schwabe B., Hložek R., Marsh D. J. E., Rogers K. K., 2024, Phys. Rev. D, 109, 043507
Levkov D., Panin A., Tkachev I., 2017, Phys. Rev. Lett., 118, 011301
Li B., Rindler-Daller T., Shapiro P. R., 2014, Phys. Rev. D, 89, 083536
Li B., Shapiro P. R., Rindler-Daller T., 2017, Phys. Rev. D, 96, 063505
Li X., Hui L., Yavetz T. D., 2021, Phys. Rev. D, 103, 023508
Lora V., Magaña J., 2014, J. Cosmol. Astropart. Phys., 2014, 011
Luu H. N., Tye S. H. H., Broadhurst T., 2020, Phys. Dark Universe, 30, 100636
Luu H. N., Mocz P., Vogelsberger M., May S., Borrow J., Tye S. H. H., Broadhurst T., 2024, MNRAS, 527, 4162
Marsh D. J. E., 2016, Phys. Rep., 643, 1
Marsh D. J. E., Pop A.-R., 2015, MNRAS, 451, 2479
Matos T., Ureña-López L. A., Lee J.-W., 2024, Front. Astron. Space Sci., 11, 1347518
May S., Springel V., 2021, MNRAS, 506, 2603
Mocz P., Vogelsberger M., Robles V. H., Zavala J., Boylan-Kolchin M., Fialkov A., Hernquist L., 2017, MNRAS, 471, 4559
Mocz P. et al., 2019, Phys. Rev. Lett., 123, 141301
Mocz P. et al., 2020, MNRAS, 494, 2027
Mocz P. et al., 2023, MNRAS, 521, 2608
Moore B., 1994, Nature, 370, 629
Moore B., Ghigna S., Governato F., Lake G., Quinn T., Stadel J., Tozzi P., 1999, ApJ, 524, L19

Navarro J. F., Frenk C. S., White S. D. M., 1996, ApJ, 462, 563
Niemeyer J. C., 2020, Prog. Part. Nucl. Phys., 113, 103787
Nori M., Baldi M., 2021, MNRAS, 501, 1539
Nori M., Murgia R., Iršič V., Baldi M., Viel M., 2019, MNRAS, 482, 3227
Oman K. A. et al., 2015, MNRAS, 452, 3650
Padilla L. E., Rindler-Daller T., Shapiro P. R., Matos T., Vázquez J. A., 2021, Phys. Rev. D, 103, 063012
Peccei R. D., Quinn H. R., 1977, Phys. Rev. Lett., 38, 1440
Roszkowski L., Sessolo E. M., Trojanowski S., 2018, Rep. Prog. Phys., 81, 066201
Safarzadeh M., Spergel D. N., 2020, ApJ, 893, 21
Sales L. V., Wetzel A., Fattahi A., 2022, Nat. Astron., 6, 897
Schaye J. et al., 2014, MNRAS, 446, 521
Schive H.-Y., Chiueh T., 2018, MNRAS, 473, L36
Schive H.-Y., Chiueh T., Broadhurst T., 2014a, Nat. Phys., 10, 496
Schive H.-Y., Liao M.-H., Woo T.-P., Wong S.-K., Chiueh T., Broadhurst T., Hwang W. Y. P., 2014b, Phys. Rev. Lett., 113, 261302
Schwabe B., Niemeyer J. C., 2022, Phys. Rev. Lett., 128, 181301
Schwabe B., Niemeyer J. C., Engels J. F., 2016, Phys. Rev. D, 94, 043513
Schwabe B., Gosenca M., Behrens C., Niemeyer J. C., Easther R., 2020, Phys. Rev. D, 102, 083518
Shapiro P. R., Dawoodbhoy T., Rindler-Daller T., 2022, MNRAS, 509, 145
Shen X. et al., 2024, MNRAS, 527, 2835
Shevchuk T., Kovetz E. D., Zitrin A., 2023, preprint (arXiv:2308.14640)
Springel V. et al., 2017, MNRAS, 475, 676
Svrcek P., Witten E., 2006, J. High Energy Phys., 2006, 051
Veltmaat J., Schwabe B., Niemeyer J. C., 2020, Phys. Rev. D, 101, 083518
Visinelli L., Baum S., Redondo J., Freese K., Wilczek F., 2018, Phys. Lett. B, 777, 64
Vogelsberger M. et al., 2014a, MNRAS, 444, 1518
Vogelsberger M. et al., 2014b, Nature, 509, 177
Vogelsberger M., Marinacci F., Torrey P., Puchwein E., 2020, Nature Reviews Physics, 2, 42
Weinberg S., 1978, Phys. Rev. Lett., 40, 223
Widrow L. M., Kaiser N., 1993, ApJ, 416, L71
Witten E., 1980, Annals of Physics, 128, 363
Woo T.-P., Chiueh T., 2009, ApJ, 697, 850
Zhang U.-H., Chiueh T., 2017, Phys. Rev. D, 96, 063522

APPENDIX A: ACCURACY OF GENERALIZED DENSITY PROFILE FITTING FORMULA

In equation (11), we propose a new fitting formula for dilute solitons under attractive self-interactions that generalizes equation (9) originally found in Schive et al. (2014a). First, we seek to identify the (a, b) parameter set that best matches solutions to the GPP equations over the relevant range of interaction strengths. We do this via an optimization process, visualized in Fig. A1. For any two values of a and b, the goodness of fit metric δ^2 from equation (27) can be used to compare our predictions to the GPP solutions across a range of β values. The total accuracy of an (a, b) model is simply the sum of δ^2 values over $0 < \beta < 1$. In Fig. A1, these $\sum \delta^2$ accuracy values are displayed by colour for a 20×20 grid of (a, b) values. The optimal parameter set is found to be $a = 11.2$ and $b = 4.2$, but there is a strong degeneracy between the two parameters ($a \approx 4b - 5.5$). Increasing a tends to decrease the density over the relevant range of radii, while increasing b reverses the effect. In this sense, the functional form of equation (11) admits a family of well-fitting solutions to self-interacting FDM haloes.

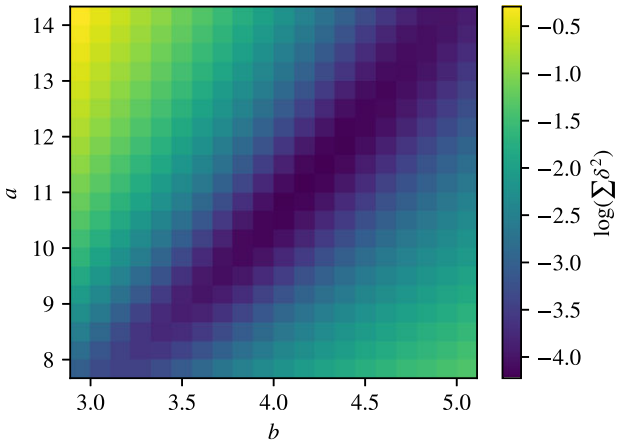

Figure A1. Goodness of fit measurement for equation (11) using many values of parameters a and b. The optimal combination is $a = 11.2$ and $b = 4.2$, and these values are set constants throughout the entire analysis.

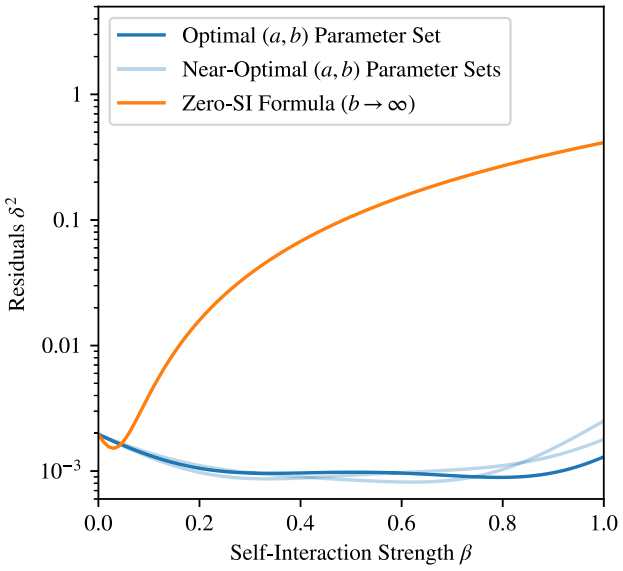

Figure A2. Comparison of goodness of fit of the zero-SI formula, equation (9) (orange), to the generalized formula, equation (11) (blue), over the relevant range of SI strengths. The soliton density profile changes subtly with self-interactions such that equation (11) yields a much more accurate description. The optimal (a, b) parameter set (11.2, 4.2) is shown as the bolded curve, but other (a, b) parameter sets lying along the degeneracy (see Fig. A1) are also included: (10.5, 3.9) and (12.5, 4.5).

To demonstrate the accuracy of our fitting formula with its optimal (a, b) parameter set, Fig. A2 plots the residuals δ^2 as a function of β. Also included are residual functions for the zero-SI formula, equation (9), and two nearly-optimal (a, b) parameter sets that lie along the degeneracy in Fig. A1. While the fit using the zero-SI formula becomes increasingly poor as the SI strength is dialed up, equation (11) offers persistently great fits to the GPP solutions. The two other (a, b) parameter sets shown, (10.5, 3.9) and (12.5, 4.5), exhibit only marginally worse residuals at high β.

APPENDIX B: GENERALIZED SOLITON MASS FORMULA

In equation (20), we assert that the formula for the mass of dilute solitons under attractive self-interactions is only off by a multiplicative function $g(\beta)$ from the analytic zero-SI formula, equation (18).

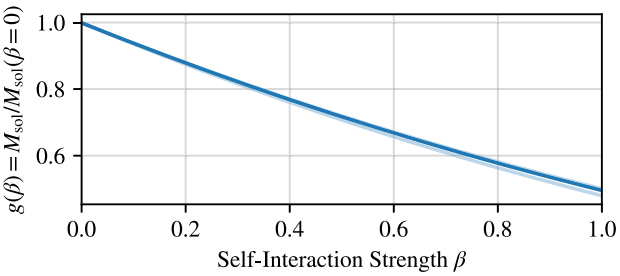

Figure B1. The residual dependence of the soliton mass on self-interaction parameter β after normalizing by the zero-SI case. Increasing self-interaction strength decreases the soliton mass relative to the zero-SI prediction. As in Fig. A2, the optimal (a, b) parameter set is represented by the bold blue curve, while two other well-fitting parameter sets are shown in faded blue. Changing parameter sets along the degeneracy shown in Fig. A1 changes $g(\beta)$ only very slightly.

To see this, let $u = r/r_{\rm c}$ so that

$$M_{\rm sol} = \int_0^\infty 4\pi r^2 \rho_{\rm sol}(r) {\rm d}r = 4\pi\rho_0 r_{\rm c}^3 \int_0^\infty \frac{u^2\,{\rm d}u}{\left[1 + A(\beta)u^{B(\beta)}\right]^8}$$

where $A(\beta) = 0.091a^{\beta/b}$ and $B(\beta) = 2 - \beta/b$. In this form, it is clear that $M_{\rm sol} \propto \rho_0 r_{\rm c}^3 \propto r_{\rm c}^{-1}$ regardless of SI strength. The multiplicative function $g(\beta)$ is proportional to the above integral,

$$g(\beta) = \frac{M_{\rm sol}(\rho_0, \beta)}{M_{\rm sol}(\rho_0, 0)} = \frac{4096A(0)^{3/2}}{33\pi} \int_0^\infty \frac{u^2\,{\rm d}u}{\left[1 + A(\beta)u^{B(\beta)}\right]^8},$$

which cannot be expressed in terms of elementary functions except in special cases. A plot of $g(\beta)$, computed with numerical integration, is shown in Fig. B1 for different (a, b) parameter sets. The soliton mass under strong self-interactions can be less than 60 per cent of the mass predicted from the zero-SI formula.

APPENDIX C: SPECTRAL METHOD

To evolve and merge the haloes, we numerically solve equations (14) and (2) following the spectral method as developed and used in Mocz et al. (2017). The time-steps are decomposed into a kick-drift-kick leapfrog-like scheme, where each 'kick' and 'drift' are unitary operators acting on the wavefunction. The sequence is briefly reviewed here.

Once the density ρ and wavefunction ψ are discretized onto a grid of dimension N^3, the potential V can be calculated by transforming to Fourier space and back,

$$V = {\rm ifft}\left[-{\rm fft}[4\pi G(\rho - \bar{\rho})]/k^2\right], \tag{C1}$$

where fft[...] and ifft[...] are the Fourier transform and inverse Fourier transform operators, respectively, and k are the wavenumbers at the corresponding grid locations. The potential imparts a 'kick' to the wavefunction, half a time-step forward,

$$\psi \leftarrow \exp\left[-i(\Delta t/2)(m/\hbar)V\right] \cdot \psi. \tag{C2}$$

This is followed by a full 'drift' (kinetic) step in Fourier space:

$$\hat{\psi} = {\rm fft}[\psi] \tag{C3}$$

$$\hat{\psi} \leftarrow \exp\left[-i\,\Delta t(\hbar/m)k^2/2\right] \tag{C4}$$

$$\psi \leftarrow {\rm ifft}[\hat{\psi}]. \tag{C5}$$

The time-step is completed with another 'kick' step using equation (C2), except that the interaction terms from equation (14) are included in the potential,

$$V \leftarrow V - \frac{4\pi\hbar^2 a_{\rm s}}{m^3}|\psi|^2 + \frac{32\pi\hbar^4 a_{\rm s}^2}{3m^6c^2}|\psi|^4 \tag{C6}$$

and the system is thus evolved from time t to $t + \Delta t$.

The valid time-step criterion for stability and accuracy of our method, essentially a Courant–Friedrichs–Lewy (CFL) like condition, is that the unitary operators in equations (C2) and (C4) do not change the phase by more than 2π in each time-step. The time-step criterion of Schwabe, Niemeyer & Engels (2016),

$$\Delta t \leq \max\left[\frac{m}{6\hbar}(\Delta x)^2, \frac{h}{m\max|V|}\right] \tag{C7}$$

enforces this property, where $\Delta x = L/N$ is the grid spacing. Note that the time-step scales as $(\Delta x)^2$, which adds computational cost for high-resolution simulations.

This paper has been typeset from a TEX/LATEX file prepared by the author.